Role of annealing and photostability of mixed halide organo-metal-halide semiconductors for solar cell applications

by

David Sörell

Department of Chemical Physics
Lund University

November 2015

Supervisor: **Postdoc Eva Unger**
Examiner: **Professor Sven Lidin**

Postal address
Chemical Physics
P.O. Box 124
SE-22100 Lund, Sweden

Visiting address
Getingevägen 60

Web address
www.chemphys.lu.se

Abstract

Methyl ammonium lead halides ($MAPbX_3$, $X=Cl^-$, Br^-,I^-), crystallizing in a perovskite structure, have in recent years been shown to be a promising material as a light harvesting material in solar cells. It has many interesting properties which makes it suitable for solar cell applications, such as near-optimal band gap and long electron-hole diffusion lengths, as well as the possibility of synthesizing the films from solution based methods. It is also possible to tune the band gap by making mixed compounds of $MAPb(I_{1-x}Br_x)_3$ ($0 \leq x \leq 1$), which could make this compound suitable for tandem cell applications. In order to optimize these perovskites for tandem cells, there are many steps and properties that need investigation. In this work, band gap tuning and structural properties were investigated using both optical techniques such as UV-Vis and Photoluminescence, as well as X-Ray Diffraction. Furthermore, the effect of annealing was studied by making measurements before and after annealing. Also, theoretical calculations of tandem cells were done to find the optimal band gap for $MAPb(I_{1-x}Br_x)_3$.

Bang gap tuning was achieved for $MAPb(I_{1-x}Br_x)_3$ and the most efficient composition was calculated to $MAPbI_{1.05}Br_{1.95}$. Studies of annealing showed that the band gap onset becomes sharper after annealing. Peaks in XRD also became narrower, indicating either more homogenous samples or larger crystallite size.

When $MAPb(I_{1-x}Br_x)_3$ is illuminated with light, a phase splitting occurs creating multiple band gaps. This may be a problem for tandem cells, since the optimal band gap is not stable. Due to the phase splitting, a 4-terminal solar cell may be the preferred choice since the efficiency calculations show that the efficiency is less prone to change as the band gap is varied. Developing stable $MAPb(I_{1-x}Br_x)_3$ is necessary to produce efficient tandem solar cells.

Sammanfattning

Metylammonium-bly-halider ($MAPbX_3$, $X=Cl^-$, Br^-,I^-), som kristalliserar i en perovskitstruktur, har de senaste åren visat sig vara ett lovande material för solceller. Det har många intressanta egenskaper som gör det passande för solceller, såsom ett optimalt bandgap och lång elektron/hål-diffusionslängd, samt möjligheten att tillverkas genom lösningsbaserade metoder. Det är också möjligt att justera bandgapet genom att tillverka föreningar med både brom och jod, $MAPb(I_{1-x}Br_x)_3$ ($0 \leq x \leq 1$), vilket gör det här materialet passande för tandemsolceller. För att optimera dessa föreningar för tandemsolceller är det många egenskaper som behöver undersökas. I det här arbetet har bandgapet samt strukturella egenskaper undersökts med både optiska metoder som UV-Vis och fotoluminiscens, samt röntgendiffraktion (XRD). Dessutom har uppvärmningssteget undersökts genom att utföra mätningar före och efter uppvärmning. Till sist har teoretiska beräkningar av tandemceller utförts för att hitta det optimala bandgapet för $MAPb(I_{1-x}Br_x)_3$.

Justering av bandgapet för $MAPb(I_{1-x}Br_x)_3$ utfördes och den mest effektiva sammansättningen beräknades till $MAPbI_{1.05}Br_{1.95}$. Studier av uppvärmningen visade att bandgapets ansats blir skarpare efter uppvärmning. Dessutom blev topparna i XRD smalare, vilket tyder på att proven antingen blivit mer homogena eller att kristallstorleken ökat.

När $MAPb(I_{1-x}Br_x)_3$ belyses med ljus sker en fasseparation vilket skapar multipla bandgap. Denna egenskap är ett problem för tandemsolceller, eftersom att det optimala bandgapet inte tycks vara stabilt. På grund av fasseparationen är troligtvis en tandemcell med fyra terminal att föredra, eftersom att de teoretiska beräkningarna visar att verkningsgraden för en fyrterminal förändras mindre med bandgapet. Att utveckla stabila filmer av $MAPb(I_{1-x}Br_x)_3$ är nödvändigt för att i framtiden kunna tillverka stabila tandemsolceller.

Contents

1. Introduction

1.2 Background

Methyl ammonium lead halides, $MAPbX_3$, have in recent years proved to be a promising material for solar cell applications, giving efficiencies around 20 % [1][2]. They exhibit many properties that make them suitable for solar cells, such as optimal band gaps[3], long electron-hole diffusion lengths[4][5]. They can also be produced from solution based methods which is a cheaper alternative compared to many other methods[6][7]. The possibility of using these compounds for tandem solar cells is currently being investigated. Especially the possibility to couple these solar cells with InP nanowire solar cells has been investigated [8].One way of doing this would be to tune the band gap by having mixed halide compounds, $MAPb(X_{1-x}Y_x)_3$. Band gap tuning of $MAPb(I_{1-x}Br_x)_3$ has in previous work been achieved by Noh et al.[9] and their article is what this work is a continuation of. There are still many problems with these mixed halide compounds, for example to synthesize films that are photostable, which has been reported by Hoke et al.[10].

1.1 Aim

The aim of this thesis is to continue on previous work on mixed halide perovskites in order to get a better understanding of the processes occurring in the material. Especially, the annealing step will be investigated to find out how annealing affects the properties of the material. The techniques used involve optical techniques such as UV-Vis spectroscopy and Photoluminescence, and also X-Ray Diffraction. Furthermore, the possibility of using mixed halide perovskites for tandem solar cells is investigated.

2. Theoretical Background

2.1 Methyl ammonium lead halides ($MAPbX_3$)

The methyl ammonium lead halides belong to a group of compounds also known as Organic-Inorganic Perovskites (OIP). They have the general chemical formula ABX_3, where A can be a monovalent organic cation, such as formamidinium (FA) or methylammonium (MA), B is a divalent metal cation such as Pb^{2+} or Sn^{2+}, and X is a halide anion (Cl^-, Br^-, I^-). What they have in common is that they all crystallize in a perovskite-like structure, although the space group may vary between the compounds. For this reason, the compounds are sometimes called “perovskites” for short. The structure consists of two cations, $CH_3NH_3^+$ (MA) and Pb^{2+}. In a cubic lattice, the lead ion is situated at the body centre position (½, ½, ½) and the methyl ammonium ions are located at all the cubic corner positions (0, 0, 0). The halides are found at the face centred positions (½, ½, 0). The lead ion has a 6-fold coordination, being encased by an octahedron of halide ions. The methyl ammonium ion is coordinating 12 halide ions in the shape of a cuboctahedron. The structure is in some cases distorted, depending on the size of the anion. This causes the unit cell to become tetragonal instead of cubic, which will be described later on.

There are many reasons as to why OIPs have become subject to extensive research in recent years. Perovskites have proven to be a promising material for solar cell applications, where solar cells using $MAPbI_3$ as a light harvester quickly have reached efficiencies around 20 %[1][2]. $MAPbI_3$ has many properties which makes it suitable as a light-absorbing material in solar cells. The band gap of $MAPbI_3$ is 1.55 eV, which is close to the optimal band gap of 1.34 eV as calculated from the Shockley-Quessier limit[3]. They also have a high absorption coefficient, which means they absorb most of the light with energy larger than the band gap.

Another property that makes $MAPbI_3$ interesting for solar cell applications is the long diffusion length of electrons and holes, which is the distance the electrons and holes are able to travel through the material before recombining. It is necessary to have a long enough diffusion length so that the charges can be separated and extracted[4][5]. Methyl ammonium lead halides are also easy to deposit and the materials needed are abundant and relatively cheap compared to many other solar cell materials, for example crystalline silicon and III-V semiconductors. They can be deposited by spreading a solution of the constituent precursor salts on a substrate by spin-casting. Excess solvent either evaporates during spin-casting or the subsequent drying or annealing step[6][7].This technique is called spin-coating and was used throughout this work to form the films.

Because of the large size of I^-, 2.2 Å, $MAPbI_3$ is unable to crystallize in a cubic perovskite structure. Instead, the octahedrons formed by the anions are distorted and angled. This causes the unit cell to become tetragonal, with space group I4/mcm. The lattice parameters for $MAPbI_3$ are c=12.71 Å and a=8.81 Å. The unit cell of $MAPbI_3$ can be imagined as being built out of 8 sub-cells in a 2x2x2 order. It requires two lead atoms in the c direction as well as a and b to describe the complete unit cell.

Instead of crystallizing in a tetragonal perovskite structure like $MAPbI_3$, $MAPbBr_3$ crystallizes in a cubic perovskite structure of space group $Pm\bar{3}m$[11]. The distorted octahedrons in $MAPbI_3$ are now organized in a symmetric way and allows the formation of a cubic structure. $MAPbBr_3$ has a higher band gap than its iodide counterpart, 2.35 eV [12]. This band gap in itself is not optimal for single junction solar cells, but still devices have been made with 10.4 % efficiency, based purely on $MAPbBr_3$ as the light absorbing material[13].

2.2 Mixed halide compounds, $MAPb(X_{1-x}Y_x)_3$

So far, only perovskites which includes one halide have been described. However, it is possible to mix halides in almost any proportion, to form $MAPb(X_{1-x}Y_x)_3$, where X is one halide and Y another halide and $0 \leq x \leq 1$. This has made it possible to improve many important properties of the solar cells. For example, $MAPbCl_3$ has no direct application as a light absorbing material due to its high band gap of 3.0 eV which only is able to generate a very small photocurrent. Still, adding chloride to $MAPbI_3$ has been shown to increase the diffusion length of electron and holes to over a micron[4]. Solar cells have been made using $MAPb(I_{1-x}Cl_x)_3$with efficiencies near 20 %. However, the amount of Cl is very small as it evaporates as MACl during annealing [14].

It is also possible to substitute iodide with bromide in the perovskite structure. When just a small amount of bromide is present, the structure remains in the tetragonal structure of $MAPbI_3$. As more bromide is added, the perovskite does not split into a cubic and a tetragonal phase. Instead, a transition to the cubic structure starts to occur when there is around 20 % bromide, which remains as the composition reaches $MAPbBr_3$. The lattice parameter of $MAPb(I_{1-x}Br_x)_3$ can be approximated using Vegard's Law, which states that for a given random alloy AB_xC_{1-x}, the lattice parameter of the alloy can be described by a linear interpolation between the two elements B and C[15]. This approximation is valid if the crystal structure remains the same, which is not the case for $MAPb(I_{1-x}Br_x)_3$ where it transitions from a tetragonal structure to a cubic structure around x = 0.2. Therefore, there are two linear regions where one ranges from x = 0 to x ≈ 0.2 and the other when x > 0.2 [9].

$$a_{alloy} = xa_B + (1 - x)a_C$$

2.2.2 Bandgap tuning in mixed halide $MAPb(X_{1-x}Y_x)_3$ semiconductors

Varying the amount of bromide in the perovskite also changes the band gap of the sample. It can adopt any value between the band gap of $MAPbI_3$, 1.55 eV, and $MAPbBr_3$, 2.35 eV, as the ratio between

bromide and iodide changes. The possibility of band gap tuning of $MAPb(I_{1-x}Br_x)_3$ makes this compound interesting for tandem solar cell applications, where the band gap of one cell may need to assume a certain value for optimal efficiency[9]. The band gap for an alloy AB_xC_{1-x} can be described similarly to Vegard's Law, but instead of a linear relationship there is a quadratic formula including a bowing parameter, *b* [16].

$$E_g^{AB_xC_{1-x}} = xE_g^B + (1-x)E_g^C - bx(1-x)$$

Which in the case of $MAPb(I_{1-x}Br_x)_3$:

$$E_g^{MAPb(I_{1-x}Br_x)_3} = xE_g^{MAPbBr_3} + (1-x)E_g^{MAPbI_3} - bx(1-x)$$

Rearranging gives:

$$E_g^{MAPb(I_{1-x}Br_x)_3} = bx^2 + \left(E_g^{MAPbBr_3} - E_g^{MAPbI_3} - b\right)x + E_g^{MAPbI_3}$$

2.3 Photovoltaic Cells (Solar Cells)

A photovoltaic cell converts the energy of the sun's light into electrical energy. A photon is absorbed in a semiconductor by exciting an electron in the material from the valence band where it is bound, to the conduction band where it can move freely. This process has now created a free electron and a positive hole. Usually, in regular semiconductors, the excited electron will relax back to its ground state and recombine with the hole, releasing a photon in the process and hence the energy is lost. In a photovoltaic cell however, the electron and hole can be separated by having an imbalanced electric field within the semiconductor. The electron is inserted into an external circuit where it can perform work due to its excited state, or potential difference. After the external circuit, it reaches the bottom contact of the solar cell where it recombines with a hole, completing the cycle[17][18].

The voltage of a solar cell is directly related to the band gap of the material. If the band gap is large, each excited electron will have a larger potential and hence the voltage will become large. Usually, the voltage is around 0.3-0.5 eV less than the band gap due to various losses. At the largest possible band gap, no photon will have enough energy to excite an electron, leading to a current of 0. The potential at this point is called the open circuit voltage, V_{oc}.

All photons that have an energy larger than the band gap have the potential to excite an electron. This means that the current depends on the amount of photons that excite an electron. If the band gap is 0, all photons can create an electron, giving the maximum current, J_{sc}. However, at this point there is no electric potential since the band gap is 0 and hence short circuited.

The efficiency of the solar cell is calculated with:

$$\eta = \frac{J_{sc}V_{oc}FF}{P_s}$$

Where P_s is the total power of the light source and FF is known as the fill factor and is the ratio between the maximum power point (J_mV_m) and the product of J_{sc} and V_{oc}. In this report FF is assumed to have a value of 0.7.

$$FF = \frac{J_mV_m}{J_{sc}V_{oc}}$$

2.3.1 Limiting Efficiency

It is not possible for a solar cell with a single absorption layer to convert all of the sunlight to electrical power. The theoretical limit efficiency for a single junction is called the Shockley-Quessier limit and depends on the band gap of the semiconductor[19]. There are many factors that limit the theoretical efficiency of a solar cell, including spectral losses, recombination and blackbody radiation. Out of these, spectral losses accounts for a majority of the total loss in efficiency. When a photoelectron in a semiconductor is excited to the conduction band, the electron quickly dissipates energy until it reaches the edge of the conduction band. This means that any excess energy from the absorbed photon will be lost. The consequence of this is that all photons with higher energy than the band gap energy can only use the band gap energy to contribute to the photocurrent, while the rest is lost in other processes. Another part of the spectral losses is the fact that photons with lower energy than the band gap cannot create photoelectrons and that energy will therefore not be absorbed[20].

The band gap of the solar cell dictates how large the total spectral losses will be. A small band gap will produce a large current, since more photons have enough energy to produce a photoelectron. The maximum possible current is the integrated spectrum of the light source, in this case the AM1.5 solar spectrum. However, a lot of energy will be lost when the electrons dissipate their energy to the conduction band edge, and will therefore give a low voltage. If the band gap instead is large, not many photons will have the required energy and cannot be absorbed, which results in a lower current but a high voltage. Because the final power is a product of current and potential, it is necessary to have both a high current and potential.

Blackbody radiation of the solar cell also accounts for a significant part of the efficiency loss. Because the solar cell has a working temperature it will emit blackbody radiation in the process, which cannot be absorbed by the solar cell. Also, spectral losses in the solar cell causes the solar cell to heat up further, increasing the intensity of the blackbody radiation and hence a further drop in efficiency. There is also a possibility for photoelectrons to recombine with the hole in the valence band before the electron can be separated from the solar cell, releasing a photon in the process. This recombination process is another reason why the efficiency is limited, and separation of the charges must be done before they recombine. A good solar cell is therefore characterized by a long electron-hole diffusion length, that is, the length they both move within the semiconductor before recombining.

2.3.2 Multi-junction solar cells (Tandem cells)

There are ways of achieving a higher efficiency than given by the Shockley-Queisser limit. One is by using two or more light absorbing materials with different band-gaps stacked upon each other, called a multi-junction solar cell or tandem solar cell. This allows different regions of the cell to absorb different parts of the spectrum, which in turn leads to more energy converted into electricity. The top cell with a high band gap only absorbs the high energy photons, while the low energy photons are absorbed in the bottom cell with a small band gap.

The electrical energy from a tandem cell can be extracted in two principal ways. Either the top and bottom cell are connected through the same contacts, called a two-terminal, or both layers have their own sets of contacts, called a four-terminal. The easier arrangement is to couple the two cells in series, sharing the contacts to a two-terminal. The voltage is then added like in a series coupled circuit. However, this means that the lower current of the two will limit the overall current of the tandem cell. To maximize the efficiency, the current of the top and bottom cell needs to be matched[18].

The two cells in a four-terminal tandem create a voltage and current independent of each other, which means. One of the reasons for this is the amount of contact layers required between each cell, which quickly increases as more cells are added. More contact layers also give rise to more absorption in the contact layers where no photoelectrons can be produced. The contacts may also reflect or scatter the light so that it cannot be absorbed, these effects are called parasitic absorption losses. Both these factors reduces the overall efficiency of the tandem cell[21]. In this work, it is assumed that 10 % of the available photons are lost in each contact layer due to parasitic absorption losses.

2.3.2.1 Equations for 4-terminal tandems:

$$P_{tot} = P_{top} + P_{bot}$$

$$P_{top} = V_{top} J_{top} FF$$

$$P_{bot} = V_{bot} J_{bot} FF$$

The fill factor FF assumed was 0.7.

$$V = E_g - V_o$$

Where V_0 is a constant describing how much below the bandgap the potential is. In this work, V_0 is assumed to have a value of 0.5 V. The currents are independent of each other and are calculated by integrating the solar spectrum for both cells.

$$J_{top} = p_1 \int_{E_g,top}^{\infty} \phi e \, deV$$

Where p is a constant between 0 and 1 describing the amount of photons lost due to parasitic losses.

$$J_{bot} = p_2 \int_{E_g,bot}^{E_g,top} \phi e \, deV$$

2.3.2.2 Equations for 2-terminal tandems:

$$V_{tot} = V_{top} + V_{bot}$$

$$V = E_g - V_0$$

$$J_{top} = p_1 \int_{E_g,top}^{\infty} \phi e \, deV$$

$$J_{bot} = p_2 \int_{E_g,bot}^{E_g,top} \phi e \, deV$$

$$P = V_{tot} J_{min} FF$$

J_{min} is the lowest current produced by any of the two cells, and will limit the total current of the cell to this value. Using the equations for two- and four-terminal tandems, the efficiency has been simulated using MATLAB, see Figure 1. The total efficiency was calculated as a function of the band gap of the top perovskite cell. As bottom cell, the band gap of InP nanowire solar cell has been used, 1.34 eV [8].

It can be seen that a maximum efficiency of 37 % is reached at 1.96 eV for a 2-terminal, and the same efficiency at 2.20 eV for a 4-terminal.

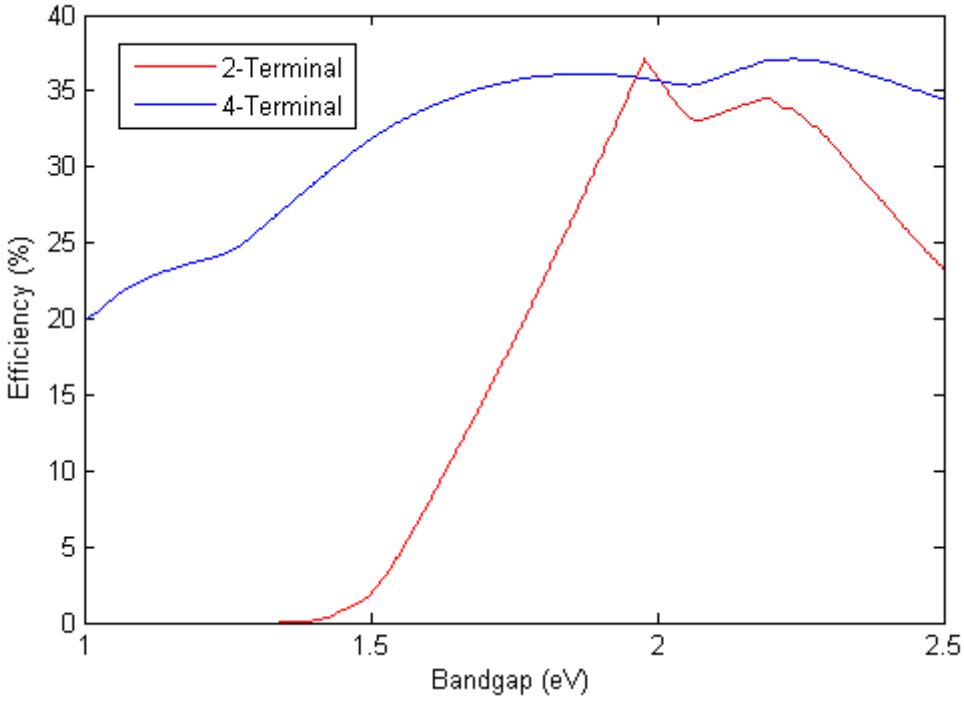

Figure 1. MATLAB simulation of the tandem efficiency as a function of the top cell band gap.

3. Techniques and Experimental

3.1 X-Ray Diffraction (XRD)

X-Ray Diffraction is a common tool for analyzing the structure of crystalline materials. A sample is irradiated with monochromatic X-rays which interacts and scatters from crystal planes in the material, changing the direction and intensity of the beam. If there is no or low energy loss during the scattering, the scattering can be described by Thompson scattering. The intensity of the diffracted beam will depend on how the X-rays interact with the crystal, which in turn depends on the atoms and how these atoms are arranged in the lattice. One special case of X-ray diffraction is when the incident beam and the lattice planes are oriented in the so called Bragg condition[22]:

$$n\lambda = 2d_{hkl} \sin \theta_B$$

Where λ is the wavelength of the X-rays, d_{hkl} the distance between lattice planes [hkl], θ_B the incident and exit angle to the lattice plane (Bragg angle), and n the order of diffraction which is an integer 0,1…,n. When the Bragg condition is fulfilled, constructive interference occurs and there will be a sharp peak in the diffraction pattern. By analyzing the angles of the Bragg peaks, the distance between lattice planes and hence interatomic distances can be determined. From this, the unit cell and crystal structure can be determined.

Most spin-coated films were analyzed with powder X-Ray Diffraction, using a STOE Stadi Mp diffractometer combined with a MYTHEN 1k detector. The X-Rays came from a copper (Kα1) source with a wavelength of 1.5418 Å. The software WinXPow was used for both the experiment and also analysis of acquired data. The scan mode was set to reflection (2θ/ω), usually ranging between 2°-90°. For calibration of the diffractometer a standard sample of silicon was used. The films were stuck to the sample holder using a silica gel and the rotation of the holder was turned on during measurements.

3.2 UV-Vis spectroscopy (UV-Vis)

One important property of semiconducting materials, such as solar cell materials, is the band gap. UV-Vis spectroscopy utilizes light in the UV/Visible/Near-infrared region of the electromagnetic spectrum to measure how light is transmitted or reflected by a sample. A monochromatic beam of light with intensity I_0 is directed at a sample, and the intensity of the light passing through is measured (I). The transmittance of the sample is given by I/I_0 and is in this report given as a percentage (%T). To measure the reflectance of the sample, the detector is put in front of the sample and again measures the intensity I. The reflectance is then given by I/I_0 and will be given as a percentage (%R) like the transmittance. From the transmittance, the absorbance of the sample can be calculated using the formula.

$$A = -\log(I_T) = -\log\left(\frac{\%I_T}{100\%}\right)$$

Because solid samples often scatter a beam of light in all directions, a small detector behind the sample to measure the transmittance would only detect a fraction of all the light transmitted through the sample. Therefore, an integrating sphere detector is used to collect the scattered light by re-reflecting it until it hits the detector. This means that the new equation for absorbance includes the reflectance of the sample in the following way[23]:

$$A = -\log\left(\frac{I_T}{I_0 - I_R}\right)$$

UV-Vis was performed using a Perkin Elmer Lambda 1050 – UV/VIS/NIR spectrometer. The detector was a Perkin Elmer – 150 mm InGaAs Integrating Sphere. The light sources were a tungsten lamp and a deuterium lamp, changing at 319.2 nm. Scans were performed from 800 nm to 250 nm with a 2 nm step size. Slit size was set to 2 nm.

3.3 Photoluminescence (PL)

While UV-Vis spectroscopy measures the absorption of light and the excitation of electrons from valence to conduction band, photoluminescence measures the photons when electrons relax from the conduction band to the valence band. By using light with higher energy than the band gap, the electrons can be excited to the conduction band and there dissipate energy until they are in the lowest possible state in the conduction band. From there they can recombine with the hole in the valence band and emit a photon, which is called radiative recombination. The energy of the radiative recombination process can be measured and the band gap determined. There is also non-radiative recombination which does not produce a photon. The energy from electron-hole recombination can be absorbed by another electron

in the conduction band, which pushes it even higher in the conduction bad where it will dissipate that energy back to the band edge, not producing a photon. This is called Auger recombination and reduces the amount of produced band gap photons in PL measurements. Photoluminescence was in this thesis used as a second method of measuring the band gap, along with UV-Vis. It was also used to investigate phase splitting of the mixed halide compositions.

Emission was performed using a Triax 320-T1 spectrograph, with a xenon lamp light source. Excitation wavelength was varied between 600 nm and 390 nm for band gap measurements and 570 nm and 440 nm for phase splitting measurements, depending on sample composition. Excitation gratings were set between 1 nm and 3 nm depending on the response of the sample. The emission slits were set to 1 nm. The emission grating was set to the approximate band gap value of the samples, or at 720 nm for phase splitting measurements. The detector was a Jobin Yvon Horiba – Symphony CCD. Integration time was 1 second for all measurements. For band gap measurements, 10 accumulations were made and averaged, while for phase splitting 60 accumulations were made and stacked.

3.4 Sample preparation

3.4.1 Spin Coating

One advantage perovskites have against many other types of solar cell materials, is that the films can be made from solution based methods. The solution based method used throughout this work is called spin-coating. The basic principle is that precursors for perovskite are dissolved in a solvent, here either γ-butyrolactone (GBL) or dimethylformamide (DMF) were used as solvents. A glass substrate is placed in a spin-coater where it is held in place using vacuum. The solution is then pipetted onto the centre of the glass substrate, whereupon the spin-coater is closed. The glass substrate is then spun at a few thousand rpm for about a minute. What happens during spinning is that the solution is thrown outward by the centrifugal force and spreads over the substrate as a thin layer. In the process, the solvent and excess material is spun is spun off and/or evaporated, and left on the substrate are the perovskite precursors which crystallizes into a thin film of perovskite. After spin-coating, the samples are annealed to both remove any residual solvent as well as speeding up the crystallization.

Because perovskites are known to be sensitive to moisture during both formation and storing, all spin-coating was done in a N_2-filled glovebox. Also, the precursors were stored in a glovebox after preparation to minimize the effect of moist air[24].

3.4.2 First set of samples

The first attempts of making perovskite films were made by weighing equimolar amounts of a lead halide, PbX_2, and methyl ammonium halide, MAX. 0.8 g PbI_2 and 0.276 g MAI were weighed and dissolved in 2 ml of GBL. Respectively, 0.637 g $PbBr_2$ and 0.194 g MABr were dissolved in 2 ml of DMF. Both solutions were stirred and heated to 60 °C for 24 hours. The stock solutions were then combined into eight solutions according to Table 1. All solutions were spin-coated at 4000 rpm for 40 seconds. After spin-coating, the samples were analyzed with UV-Vis and XRD, whereupon they were annealed at 100 °C for 10 minutes. Samples from this method turned out to be inconsistent and showed poor surface coverage. Therefore, the results are not shown from this synthesis and they are not discussed further in this report.

Table 1. Mixing scheme for the first set of samples.

$MAPbI_3$/GBL (µl)	$MAPbBr_3$/DMF (µl)	x ($MAPb(I_{1-x}Br_x)_3$)	Sample no.
200	0	0	1
150	50	0.25	2
125	75	0.375	3
100	100	0.5	4
75	125	0.625	5
50	150	0.75	6
25	175	0.875	7
0	200	1	8

3.4.3 Second set of samples

Since the first way of synthesizing films did not result in good coverage or crystallinity, another approach was tried. Equimolar amounts of MAI and PbI_2 were weighed and then added to deionized water. Due to the insolubility of $MAPbI_3$, crystals of $MAPbI_3$ quickly precipitate in the water. The solution was then vacuum filtered and the perovskite crystals cleaned with diethyl ether and thoroughly dried. The same process was repeated for MABr and $PbBr_2$ to form $MAPbBr_3$.

To make the stock solutions for spin-coating, 1.614 g of $MAPbI_3$ and 1.248 g of $MAPbBr_3$ were dissolved in 3 ml DMF each under stirring and heating to 60 °C for one hour. The stock solutions were then combined into eight solutions according to Table 2. All solutions were spin-coated at 4000 rpm for 40 seconds. After spin-coating, the samples were analyzed with UV-Vis and XRD, whereupon they were annealed at 100 °C for 10 minutes.

Table 2. Mixing scheme for the second set of samples.

$MAPbI_3$/DMF (µl)	$MAPbBr_3$/DMF (µl)	x ($MAPb(I_{1-x}Br_x)_3$)	Sample no.
200	0	0	A
150	50	0.25	B
125	75	0.375	C
100	100	0.5	D
75	125	0.625	E
50	150	0.75	F
25	175	0.875	G
0	200	1	H

4. Results and Discussion

4.1 Band gap tuning

The band-gap of the samples was determined from UV-Vis absorption spectra, as can be seen in Figure 2. From the spectra, it is clear that the band-gap increases in energy when iodide is substituted with bromide in $MAPb(I_{1-x}Br_x)_3$. From UV-Vis data, the band gap ranges from 783 nm for $MAPbI_3$ to 546 nm for $MAPbBr_3$, or 1.58 eV and 2.27 eV, which is close to the literature values of 1.55 eV and 2.30 eV. Band gap measurements from photoluminescence were inconclusive, as no clear band gap could be determined from samples with high bromide content, x = 0.625-0.875, except for pure $MAPbBr_3$. For the samples where PL measurements were successful, the method did give similar band gaps as the ones measured in UV-Vis, only slightly larger, see Figure 3. As presented in the introduction, the dependence of an alloy's bandgap on the composition can be described by the quadratic relation:

$$E_g^{MAPb(I_{1-x}Br_x)_3} = bx^2 + \left(E_g^{MAPbBr_3} - E_g^{MAPbI_3} - b\right)x + E_g^{MAPbI_3}$$

A quadratic fit was made to the UV-Vis data to give the relation (see Figure 4):

$$E_g(x) = 0.21x^2 + 0.52x + 1.6\ eV$$

The simulation of tandem-solar cells tells us that the top cell needs a band-gap of 1.98 eV to reach maximum efficiency, if the tandem cell is current matched with two terminals. This corresponds to a composition of x = 0.63 from the quadratic fit, or $MAPb(I_{0.37}Br_{0.63})_3$. However, from the tandem cell simulations it can be seen that a 4-terminal cell depends less on the band gap, it has a wider range where the efficiency is reasonably high. This allows the composition of $MAPb(I_{1-x}Br_x)_3$ to be more flexible and still give a high efficiency. Since variations in composition may occur during synthesis or decomposition, a 4-terminal may be a more stable choice of solar cell. The value of the bowing parameter is here 0.21 eV, compared to 0.33 eV which has been reported by Noh et al.[9]. A low value of the bowing parameter indicates that the miscibility of $MAPbI_3$ and $MAPbBr_3$ are highly miscible with each other[9].

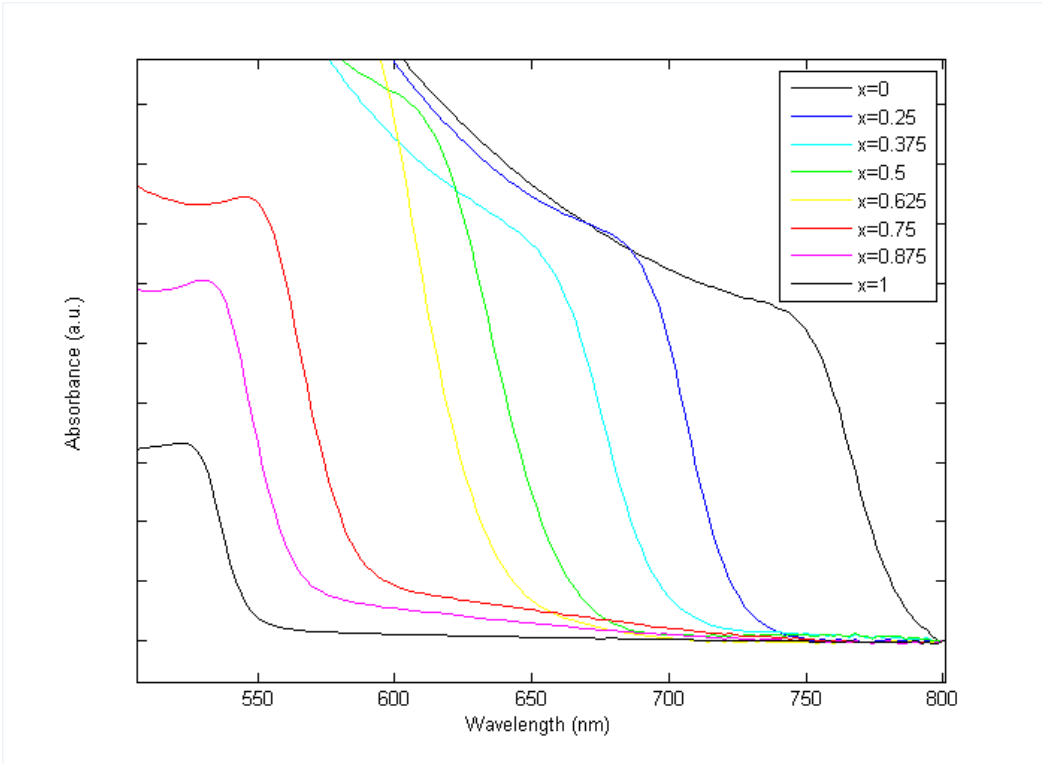

Figure 2. UV-Vis measurements after annealing for all samples. The bandgap can be seen to shift to lower wavelengths for higher x.

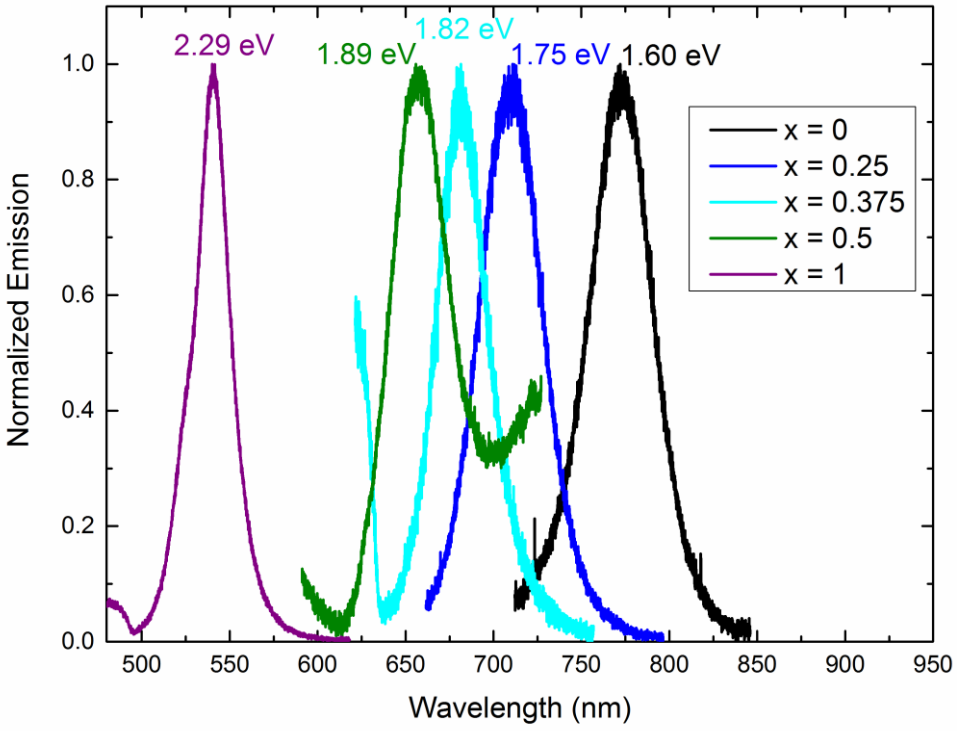

Figure 3. Bandgap measurements with PL for sample A, B, C, D and H. The band gap for sample E, F and G could not be measured with PL.

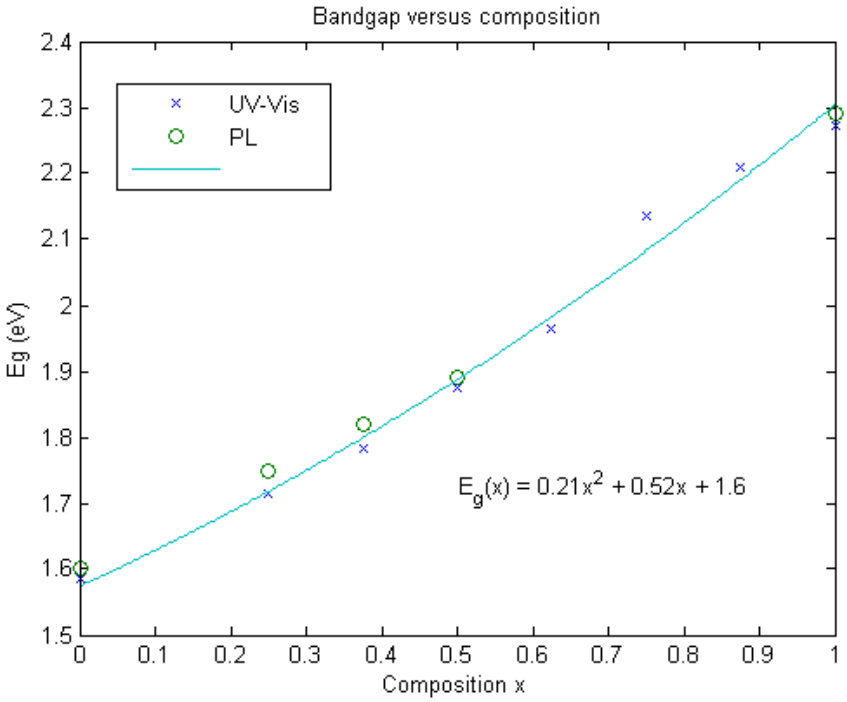

Figure 4. Bandgap as a function of composition x. The quadratic fit is made from UV-Vis data.

4.2 Lattice parameter

To study the structural change of the $MAPb(I_{1-x}Br_x)_3$ ($0 \leq x \leq 1$) series, X-Ray Diffraction (XRD) was used. First, the $MAPbI_3$ crystallizes in a tetragonal structure with lattice constants c_T=12.71 Å and a_T=8.81 Å. With these values, 2θ can be theoretically calculated for a variety of crystal planes using the formula:

$$2\theta = 2\sin^{-1}\left(\sqrt{\frac{\lambda^2}{4}\left(\frac{h^2+k^2}{a_T^2}+\frac{l^2}{c_T^2}\right)}\right)$$

and then matched with the peaks from the XRD spectrum. A summary of the relevant reflections can be seen in Table 3. Since a tetragonal structure technically has two lattice parameters, comparing the tetragonal lattice parameter to the cubic has to be done by looking at the structures. Because the tetragonal unit cell can be matched with the cubic lattice by turning it 45° and also expanding it to cover more of the cubic cells, half the c axis of the tetragonal cell matches the lattice parameter of the cubic. In the same way, $a_T/\sqrt{2}$ corresponds to a_C. By doing this, the two lattice parameters can be compared in order to get a relation between lattice parameter and composition even though the structures are different. The same procedure of theoretically calculating the diffraction angles can be done for $MAPbBr_3$, using the cubic lattice parameter a_C=5.91 Å and the cubic formula (Table 4):

$$2\theta = 2\sin^{-1}\left(\frac{\lambda}{2a_C}\sqrt{h^2+k^2+l^2}\right)$$

Table 3. Theoretical and experimental values of 2θ for different HKL of $MAPbI_3$.

2θ exp (degrees)	2θ theo (degrees)	H	K	L
14.09	14.22	1	1	0
19.98	19.96	1	1	2
28.11	28.09	0	0	4
28.42	28.66	2	2	0
31.85	32.13	3	1	0
34.94	34.82	2	0	4
40.42	40.56	2	2	4
43.04	42.93	4	1	1
50.16	50.42	4	0	4

Table 4. Theoretical and experimental values of 2θ for different HKL of $MAPbBr_3$.

2θ exp (degrees)	2θ theo (degrees)	H	K	L
14.90	14.99	1	0	0
21.15	21.26	1	1	0
25.98	26.12	1	1	1
30.09	30.24	2	0	0
33.75	33.92	2	1	0
37.07	37.27	2	1	1
45.85	46.08	3	0	0
53.48	53.73	2	2	2
62.61	62.91	4	0	0

Figure 5 below shows part of the XRD spectrum of the same series as the UV-Vis measurements. As the amount of bromide increases, the first peak is shifted from 14.1° to 14.9°. This change is not only due to a reduced lattice parameter, but also a change in crystal planes. The peak at 14.1° is calculated to be the $[110]_T$ plane for $MAPbI_3$.As bromide is added, the peak shift to 14.9° for $MAPbBr_3$. This peak is calculated to correspond to the $[100]_C$ for $MAPbBr_3$. This indicates that the lattice parameter of the compound decreases as bromide is added, assuming the planes are the same.

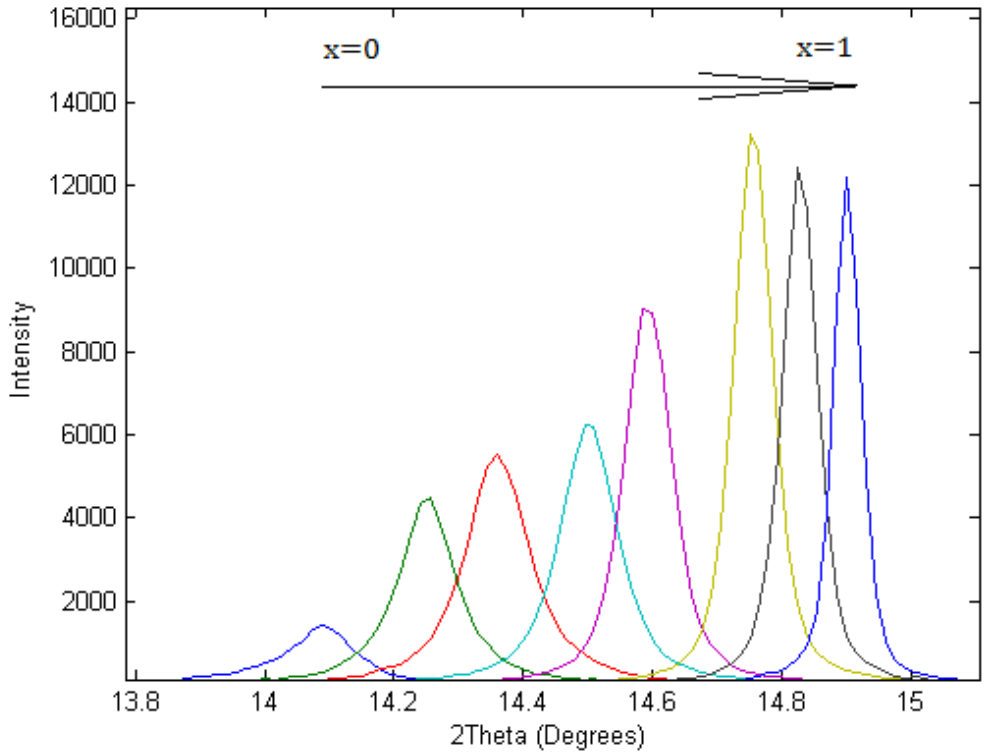

Figure 5. XRD spectra for all samples after annealing in the region 14°-15°.

$MAPbI_3$ shows two diffraction peaks around 28°, the $[004]_T$ plane at 28.1° and the $[220]_T$ plane at 28.4°, see Figure 6. When iodide is substituted with bromide, a shift of the peak is observed to 28.8°. Also, the two peaks seems to have turned into one peak instead. Because the $[200]_C$ plane of $MAPbBr_3$ is located at 30.1°, the single peak of x=0.25 at 28.8° is interpreted as a cubic $[200]_C$ peak. If the structure would still be tetragonal, two peaks would be found in close proximity which is not the case. As even more bromide is introduced, the peak keeps shifting towards $MAPbBr_3$ since Br-ions are smaller than I-ions, which reduces the lattice parameter. This shift in lattice parameter can be approximated by Vegard's Law, which states that there is a linear relationship between the lattice parameter of an alloy and the concentration of the elements it contains. This can be summarized with (Figure 7):

$$a_{alloy} = xa_A + (1 - x)a_B$$

By calculating the lattice parameter for all observed peaks and compositions, the lattice parameter, a, can be plotted against the composition, x, and a linear fit can be made to find the function describing the decrease in lattice parameter. The linear fit made here does not take the sample with x=0 into account, because of $MAPbI_3$ having another crystal structure. Deviations from the trend may be due to the stoichiometry not being exact during synthesis. In this case, a linear fit according to Vegard's Law gave:

$$a = -0.37x + 6.3 \text{ Å}$$

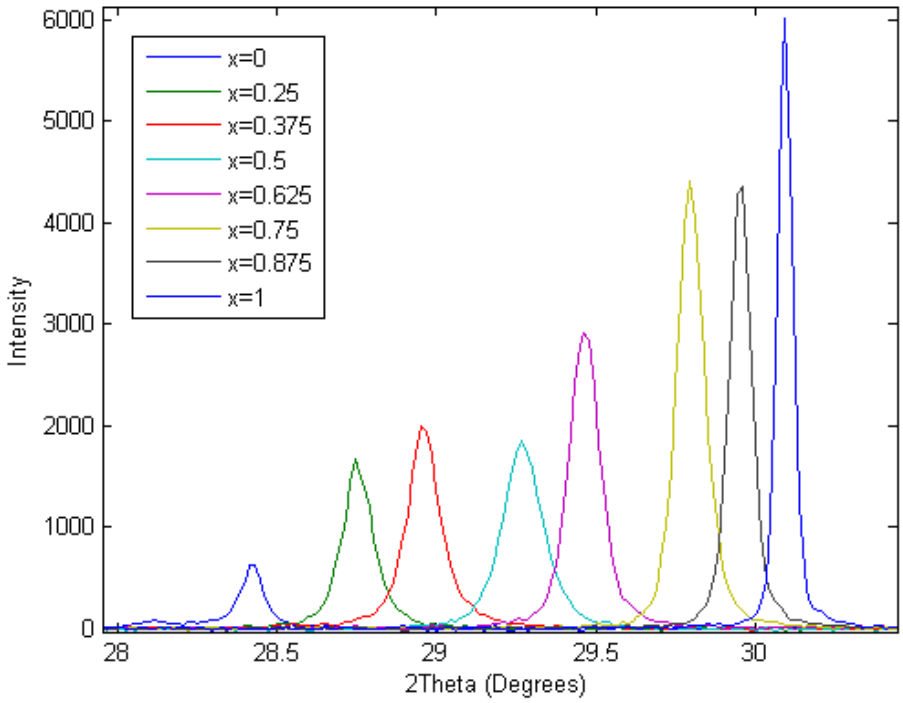

Figure 6. XRD spectra for all samples after annealing in the region 28°-31°.

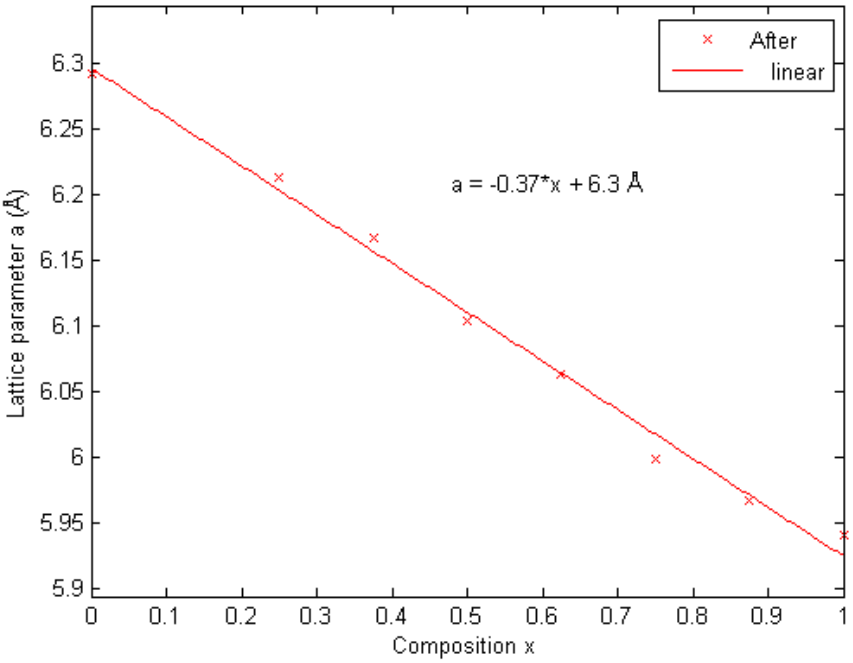

Figure 7. Lattice parameter as a function of composition x. Linear fit is made without the data point x=0.

Another point worth noting from the XRD spectra is that the width of the peak for the first mixed samples (x=0.25-0.625) is relatively large and then gets smaller for the bromide rich samples. This could mean that on short distances there are slight deviations in the composition of the films, one with more iodide and one with bromide, which would cause a spread in the peak. This feature can also be seen in the UV-

Vis spectra, where the slope onsets are not always sharp. In the case of UV-Vis it would mean there are multiple band gaps due to the inhomogeneity of the sample. Another possible explanation is that the crystallite size of bromide rich samples are smaller, hence giving narrower diffraction peaks according to the Scherrer equation.

4.3 Role of annealing after synthesis

The effect of annealing the films after spin-coating was also studied by measuring UV-Vis and XRD both before and after annealing. Fig x shows UV-Vis spectra for varying compositions before and after annealing. It can be seen that the absorbance onset is getting steeper after annealing for the mixed compositions (x=0.25-0.875), while for the pure $MAPbI_3$ and $MAPbBr_3$ the annealing appears to have little effect on the slope of the band-gap. Furthermore, the absorption spectra show a dip in absorption around 420 nm which flattens after annealing. This indicates that multiple phases form while spin-coating the solutions and that heating the samples causes these phases to combine into a more homogenous phase. Because one phase is at higher energy than the band gap and the other phase has slightly lower energy, it is likely that the high energy phase contains more bromide while the low energy phase more iodide and that the annealing causes them to mix. At the same time, the pure bromide samples appear to form $MAPbBr_3$ right after spin-coating since annealing appears to have little effect on the band-gap. Attempts were made to study the annealing process in-situ with UV-Vis using fiber optics, but the samples turned out to scatter too much light, resulting in a lot of noise and a changing baseline.

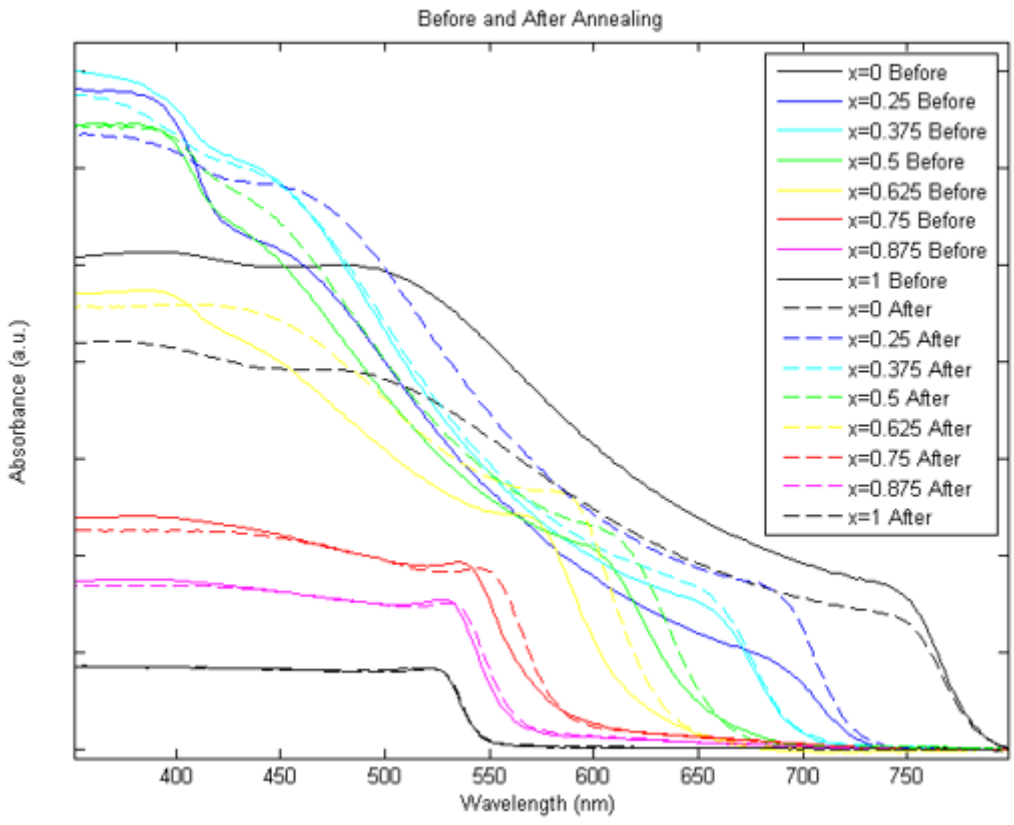

Figure 8. UV-Vis spectrum for all samples before and after annealing. It can be seen that annealing causes the band gap to be steeper and more defined.

The effects of annealing can also be seen in XRD spectra, as shown in Figure 9. For most samples (x=0.375-1) the intensity increased significantly, indicating that the films became more crystalline. The peaks also became smoother with less tailing (see x=0.375 and x=0.5). Also, the diffraction peaks were found at slightly lower angles for these samples ($\Delta 2\theta \approx 0.03$-$0.06$). This could mean that the lattice parameter increases during annealing, since larger lattices diffract X-rays at smaller angles. However, a more likely explanation is the fact that the calibration of the XRD apparatus is not perfect and also changes between samples.

The width of the peaks appears to be smaller after annealing, as seen in Figure 9. There are multiple possible explanations for this. The first is that the crystallite size has increased during annealing, which would cause XRD peaks to become narrower. Another possibility is that before annealing, the films are inhomogeneous with some regions of more bromide, and others with iodide. Small differences in composition would lead to slightly different lattice parameters, which in turn would cause XRD peaks to become broader. Annealing would then cause these regions to mix, which would homogenize the samples and cause the peaks to become narrower. This explanation also applies for the UV-Vis spectrum, where inhomogeneous samples would cause the bandgap onset to be diffuse.

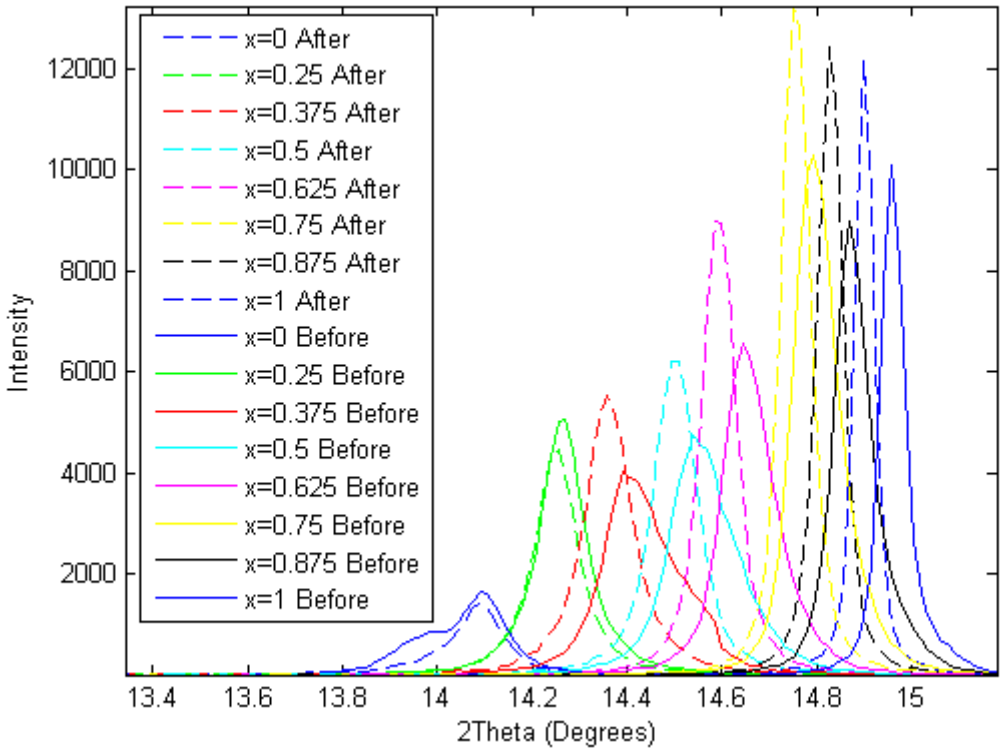

Figure 9. XRD spectra for all samples before and after annealing in the region 14°-15°.

4.4 Photoinstability of $MAPb(I_{1-x}Br_x)_3$

During photoluminescence measurements of $MAPb(I_{1-x}Br_x)_3$, the mixed bromide/iodide samples with x=0.375-0.875 show a peak between 723 nm and 745 nm that is increasing as the sample is illuminated with light, see fig x. This indicates that another phase of $MAPb(I_{1-x}Br_x)_3$ is forming when illuminated, where the iodide and bromide split into two new regions with different band gaps. It has been proposed by Hoke et al. that this is due to photo induced ion-migration[10], where halides migrate when

illuminated. It was also reported that all compositions create a low energy phase at the same energy. Here, they vary between the compositions with the lowest energy (745 nm) when x=0.5. At higher bromide content, the position of the peak gets lower with increasing bromide. Furthermore, it can be seen that the peak shifts to larger wavelengths as the sample is illuminated until it reaches a stable wavelength. This indicates that the halide migration does not occur instantaneously but instead kinetics is an important factor. This feature also appears more in samples with higher bromide content. For example, the peak in sample F with x=0.75 starts at around 715 nm and then grows gradually to 730 nm. At the same time, the peak of sample C and D (x=0.375 and x=0.5) is located at almost the same position while increasing in intensity. Apparently, samples with high bromide content take longer to reach the final wavelength of the peak while low bromide samples exhibit the same wavelength from the beginning. This suggests that it primarily could be the bromide ions that are migrating during illumination, since the new phase starts to form immediately for samples C and D but for E-G it takes a while to reach the stable energy.

Since one phase contains more iodide when illuminated, consequently there should be another phase with a higher band gap and containing more bromide. However, this phase is not visible from PL measurements because the lower band gap transitions are more likely to occur, hence hiding the high band gap phase. Sample A and H does not show this feature because they are pure iodide and bromide samples, so cannot split into multiple phases but will instead only show the band gap of the pure phase. Also sample B with x=0.25 does not show a large phase splitting, but only the band gap at 712 nm which appears to be stable.

This phase-splitting feature is most likely a problem for solar cells, since the sunlight will most likely change the band gap hence lowering the tandem efficiency. Therefore, the challenge seems to be to develop stable samples of $MAPb(I_{1-x}Br_x)_3$, perhaps by adding small amounts of another element just like chloride has been successfully added to $MAPbI_3$ to form efficient solar cells.

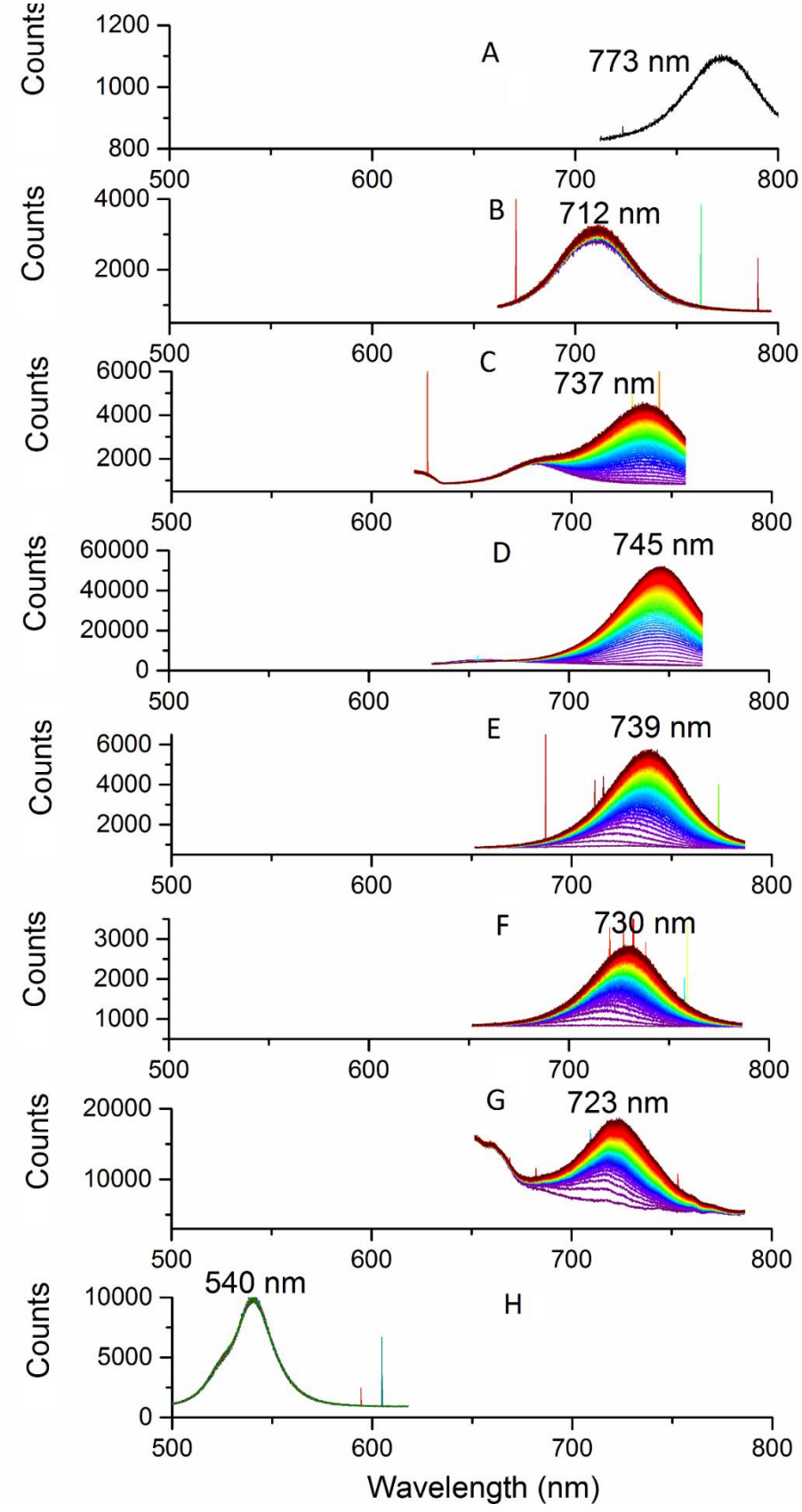

Figure 10. PL spectrum for all samples in the range 500 nm to 800 nm. A peak around 720-740 nm can be seen to increase for most samples as they are illuminated more.

5. Conclusions

It has been predicted that the optimal band gap for the $MAPb(I_{1-x}Br_x)_3$ top cell in an $InP/MAPb(I_{1-x}Br_x)_3$ tandem cell is approximately 2.0 eV, depending on whether the tandem cell is a 4-terminal or 2-terminal cell. This band gap is achieved by having a composition of approximately $MAPbI_{1.05}Br_{1.95}$. However, photoluminescence measurements show that this composition does not appear to be photostable and a new phase will form when irradiated with light. In order to make efficient solar cells, more stable compounds need to be developed.

The role of annealing in the preparation of mixed halide perovskites appears to play an important part in the formation of homogenous samples. Annealing makes the band gap steeper and more homogenous, which is important for a tandem solar cell to function more efficient. In this report, different annealing parameters were not tested in order to find an optimal method for film formation, this is instead considered future work.

6. References

[1] – Kim H, Lee C, Im J, Lee K, Moehl T, Marchioro A, Moon S, Humphry-Baker R, Yum J, Moser J.E, Grätzel M, Park N. *Lead Iodide Perovskite Sensitized All-Solid-State Submicron Thin Film Mesoscopic Solar Cell with Efficiency Exceeding 9%.* Scientific Reports. Vol 2, No. 591, 2012.

[2] – Liu M, Johnston M.B, Snaith H.J. *Efficient Planar Heterojunction Perovskite Solar Cells by Vapour Deposition.* Nature. Vol. 501, pp. 395-398, 2013.

[3] – Choi J.J, Yang X, Norman Z.M, Billinge S.J.L, Owen J.S. *Structure of Methylammonium Lead Iodide Within Mesoporous Titanium Dioxide: Active Material in High-Performance Perovskite Solar Cells.* Nano Lett. Vol. 14, pp. 127-133, 2014.

[4] – Stranks S.D, Eperon G.E, Grancini G, Menelaou C, Alcocer M.J.P, Leijtens T, Herz L.M, Petrozza A, Snaith H.J. *Electron-Hole Diffusion Lengths Exceeding 1 Micrometer in an Organometal Trihalide Perovskite Absorber.* Science. Vol 342, pp. 342-344, 2013.

[5] – Dong Q, Fang Y, Shao Y, Mulligan P, Qiu J, Cao L, Huang J. *Electron-Hole Diffusion Lengths > 175 μm in Solution-Grown $CH_3NH_3PbI_3$ Single Crystals.* Science. Vol 347, pp. 967-970, 2015.

[6] – Stranks S.D, Nayak P.K, Zhang W, Stergiopoulos T, Snaith H.J. *Formation of Thin Films of Organic-Inorganic Perovskites for High-Efficiency Solar Cells.* Angew. Chem. Int. Ed. Vol. 52, pp. 2-11, 2015.

[7] – Burschka J, Pellet N, Moon S, Humphry-Baker R, Gao P, Nazeeruddin M.K, Grätzel M. *Sequential deposition as a route to high-performance perovskite-sensitized solar cells.* Nature Vol. 499, pp. 316-319, 2013.

[8] – Wallentin J, Anttu N, Asoli D, Huffman M, Åberg I, Magnusson M.H, Siefer G, Fuss-Kailuweit P, Dimroth F, Witzigmann B, Xu H.Q, Samuelson L, Deppert K, Borgström M.T. *InP Nanowire Array Solar Cells Achieving 13.8 % Efficiency by Exceeding the Ray Optics Limit*. Science, Vol. 339, No. 6123 pp. 1057-1060, 2013.

[9] – Noh J.H, Im S.H, Heo J.H, Mandal T.N, Seok S.I. *Chemical Management for Colorful, Efficient, and Stable Inorganic-Organic Hybrid Nanostructured Solar Cells*. Nano Lett. Vol. 13, pp. 1764-1769, 2013.

[10] – Hoke E.T, Slotcavage D.J, Dohner E.R, Bowring A.R, Karunadasa H.I, McGehee M.D. *Reversible photo-induced trap formation in mixed-halide hybrid perovskites for photovoltaics.* Chem. Sci, Vol. 6, pp. 613-617, 2015.

[11] – Worhatch R.J, Kim H.J, Swainson I.P, Yonkeu A.L, Billinge S.J.L. *Study of Local Structure in Selected Organic-Inorganic Perovskites in the $Pm\bar{3}m$ phase*. Chem. Mater. Vol 20, pp. 1272-1277, 2008.

[12] – Kitazawa N, Watanabe Y, Nakamura Y. *Optical Properties of CH3NH3PbX3 (X = halogen) and their Mixed-Halide Crystals.* J. Mater. Sci., Vol 37, pp. 3583-3587, 2002.

[13] – Jeo J.H, Song D.H, Im S.H. *Planar $CH_3NH_3PbBr_3$ Hybrid Solar Cells with 10.4% Power Conversion Efficiency, Fabricated by Controlled Crystallization in the Spin-Coating Process.* Adv. Mater., Vol 26, pp. 8179-8183, 2014.

[14] – Unger E.L, Bowring A.R, Tassone C.J, Pool V, Gold-Parker A, Cheacharoen R, Stone K.H, Hoke E.T, Toney M.F, McGehee M.D. *Chloride in Lead-Chloride Derived Organo-Metal Halides for Perovskite-Absorber Solar Cells*. Chem. Mater, Vol. 26, pp. 7158-7165, 2014.

[15] – Pohl U.W. *Epitaxy of Semiconductors. Introduction to Physical Principles.* Berlin, Springer-Verlag, pp. 21-25, 2013.

[16] – Sze S.M and Lee M.K. *Semiconductor Devices: Physics and Technology*. Third Edi. New York: John Wiley & Sons, Inc, pp. 15-40, 2012.

[17] – Araújo G.L, Martí A. *Absolute Limiting Efficiencies for Photovoltaic Energy Conversion.* Solar Energy Materials and Solar Cells, Vol. 33, pp. 213-240, 1994.

[18] – Nelson J. *The Phyiscs of Solar Cells*. London: Imperial College Press, 2003.

[19] – Shockley W. and Queisser H.J. *Detailed Balance Limit of Efficiency of p-n Junction Solar Cells*. J. Appl. Phys. Vol. 32, No. 510, 1961.

[20] - Henry C.H. *Limiting efficiencies of ideal single and multiple energy gap terrestrial solar cells.* J. Appl. Phys. Vol. 51, No. 8, 1980.

[21] – Beiley Z.B and McGehee M.D. *Modeling Low Cost Hybrid Tandem Photovoltaics with the Potential for Efficiencies Exceeding 20 %.* Energy Environ. Sci. Vol. 5, pp. 9173-9179, 2012.

[22] – Bragg W.H, Bragg W.L. *The Reflexion of X-Rays by Crystals*. Proc R. Soc. Lond. A, Vol. 88, pp. 428-438, 1913.

[23] – Unger E. *XDSC: Excitonic Dye Solar Cells*. Acta Universitatis Upsaliensis. Digital Comprehensive Summaries of Uppsala Dissertations from the Faculty of Science and Technology 899. Uppsala, 2012.

[24] – Leguy A.M.A, Hu Y, Campoy-Quiles C, Alonso M.I, Weber O.J, Azarhoosh P, van Schilfgaarde M, Weller M.T, Bein T, Nelson J, Docampo P, Barnes P.R.F. *Reversible Hydration of CH3NH3PbI3 in Films, Single Crystals, and Solar Cells*. Chem. Mater. Vol. 27, pp. 3397-3407, 2015.

Appendix A. XRD spectra

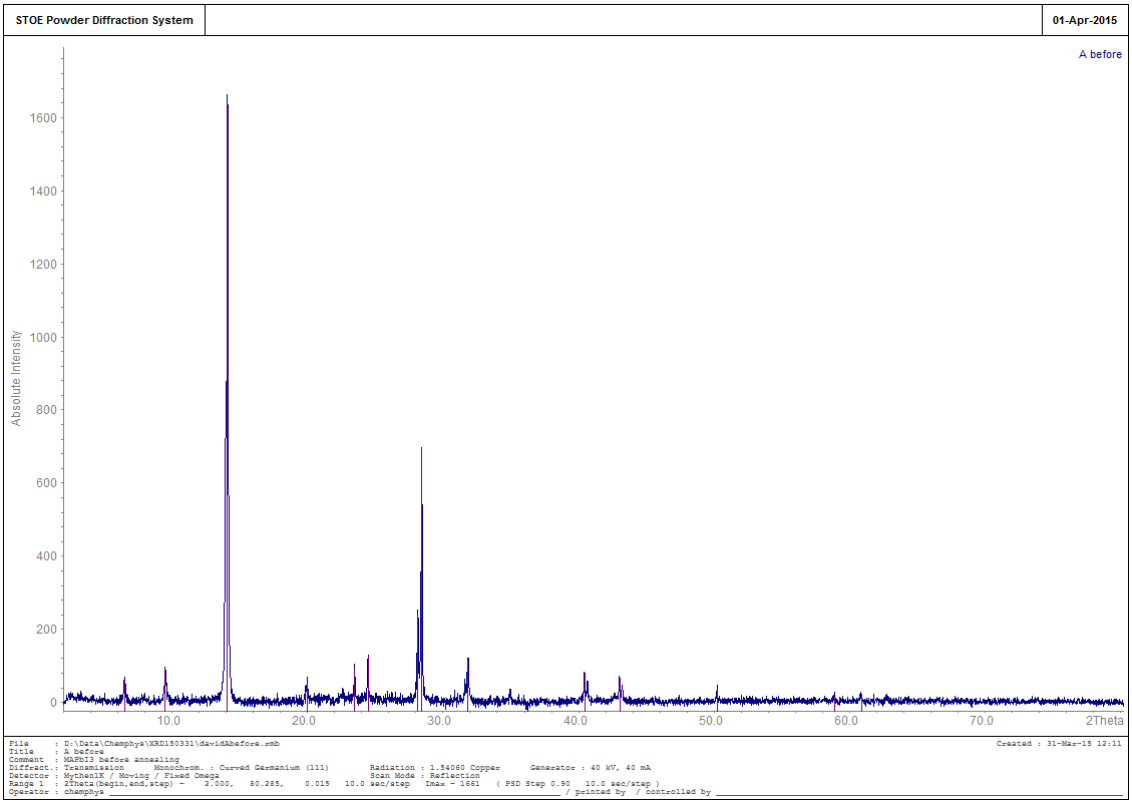

Figure A1. XRD spectrum of sample A before annealing.

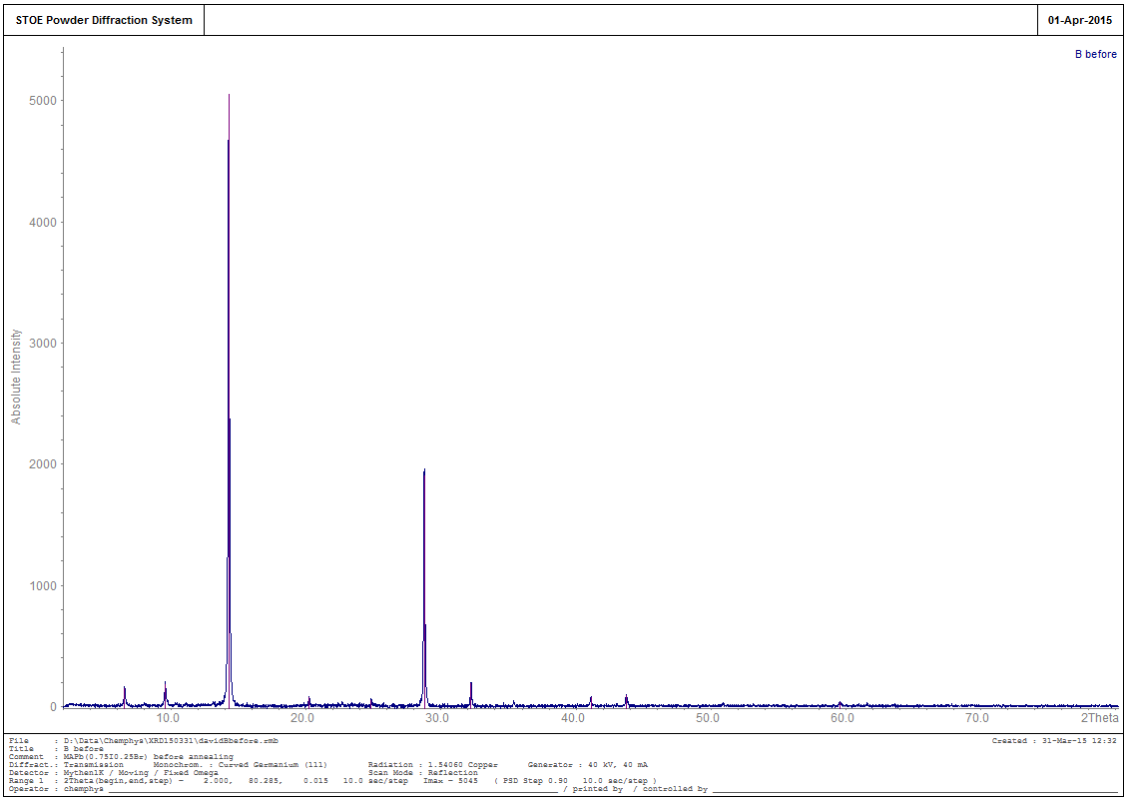

Figure A2. XRD spectrum of sample B before annealing.

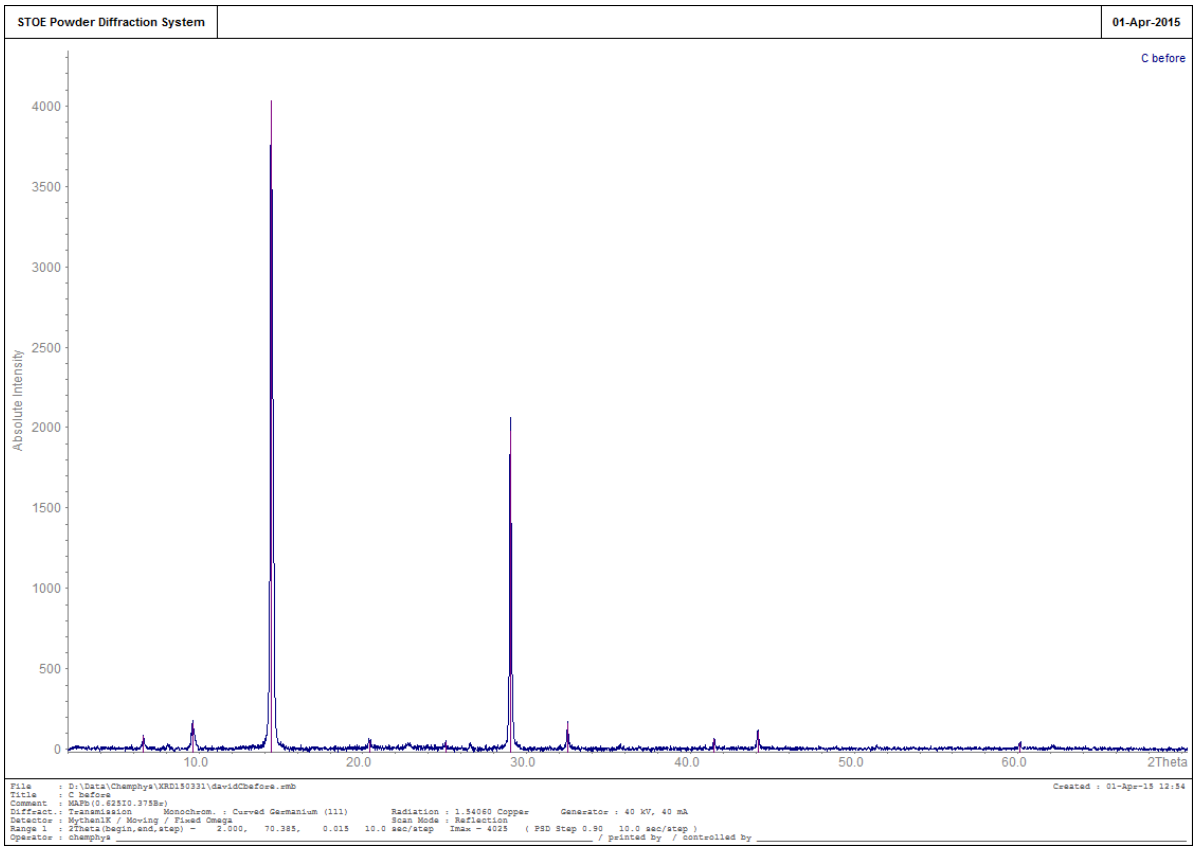

Figure A3. XRD spectrum of sample C before annealing.

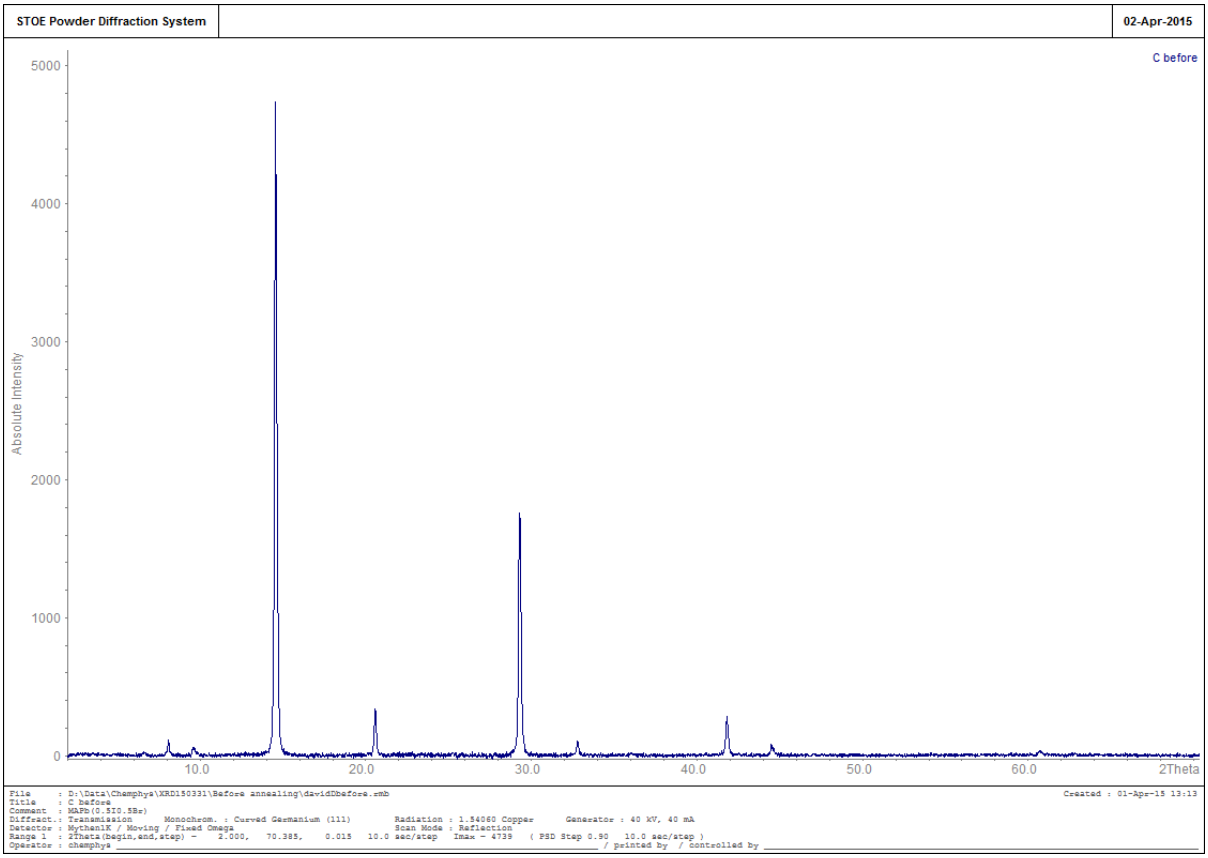

Figure A4. XRD spectrum of sample D before annealing.

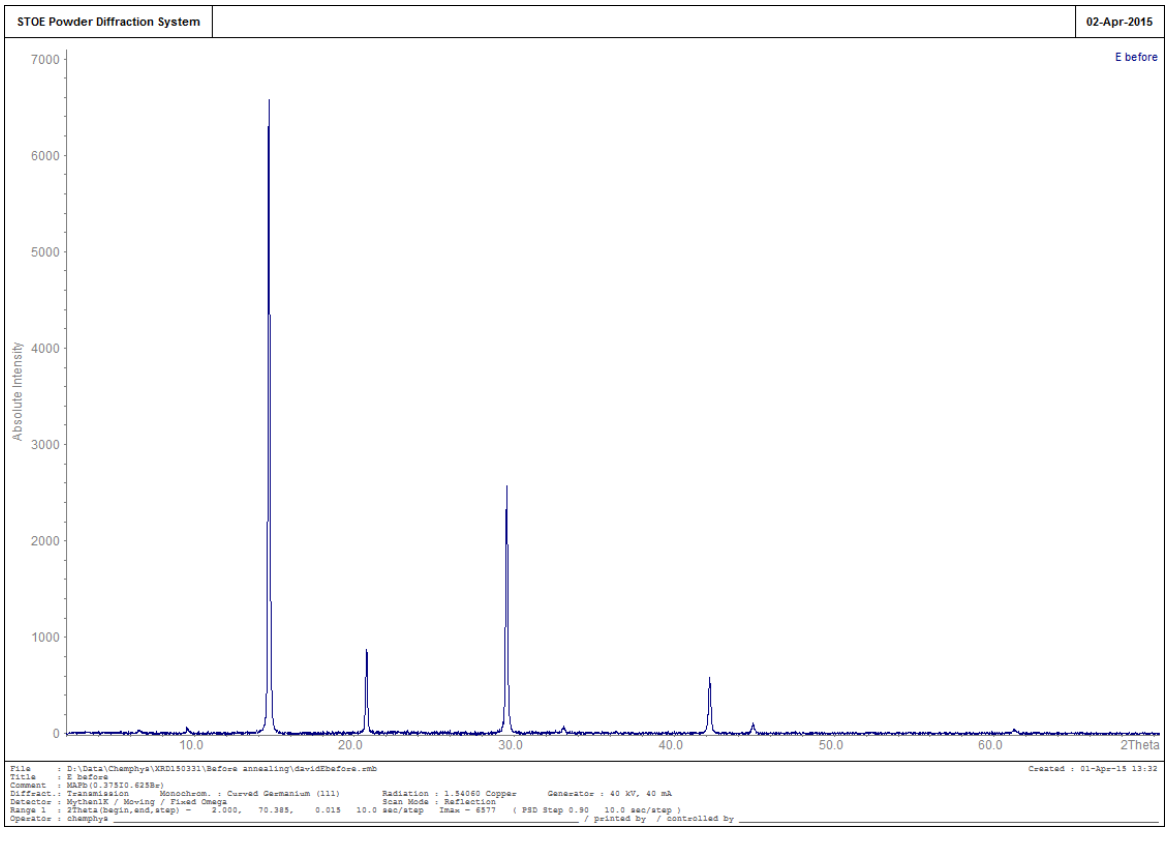

Figure A5. XRD spectrum of sample E before annealing.

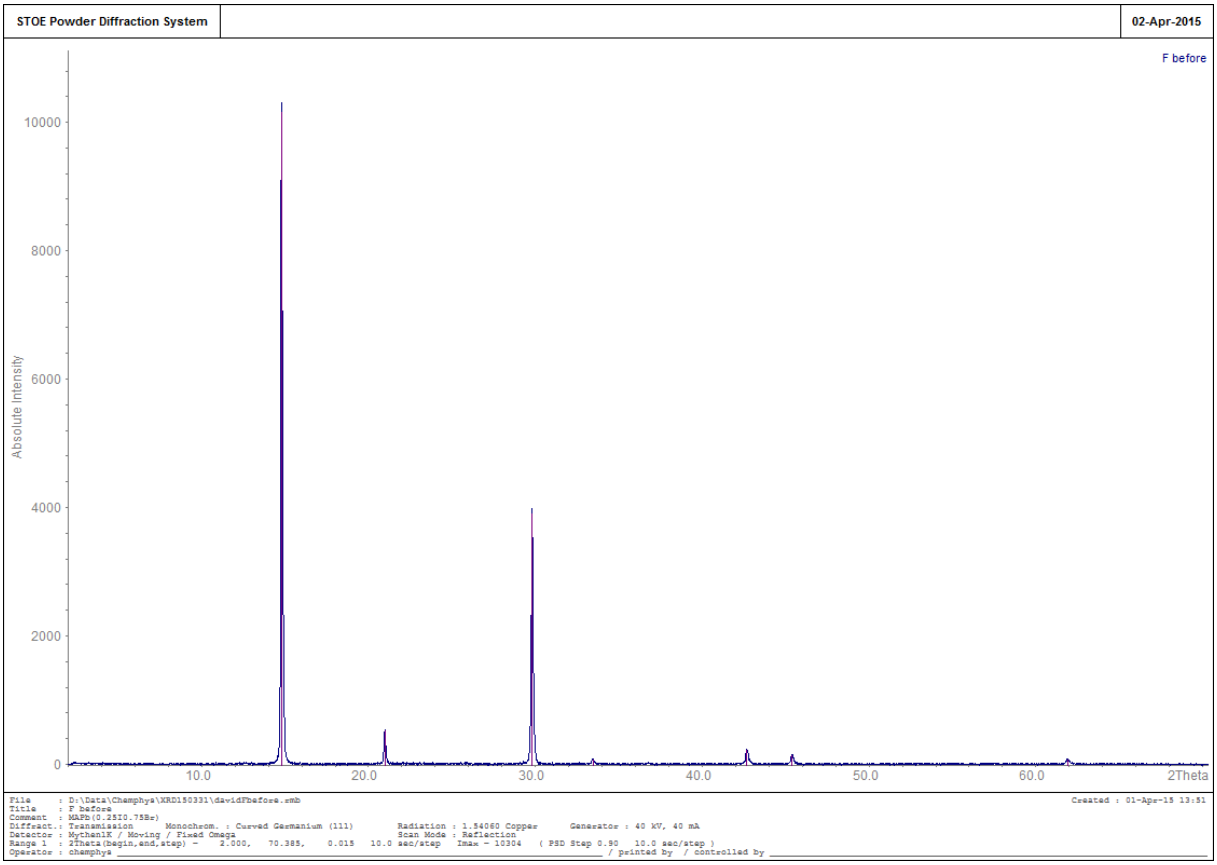

Figure A6. XRD spectrum of sample F before annealing.

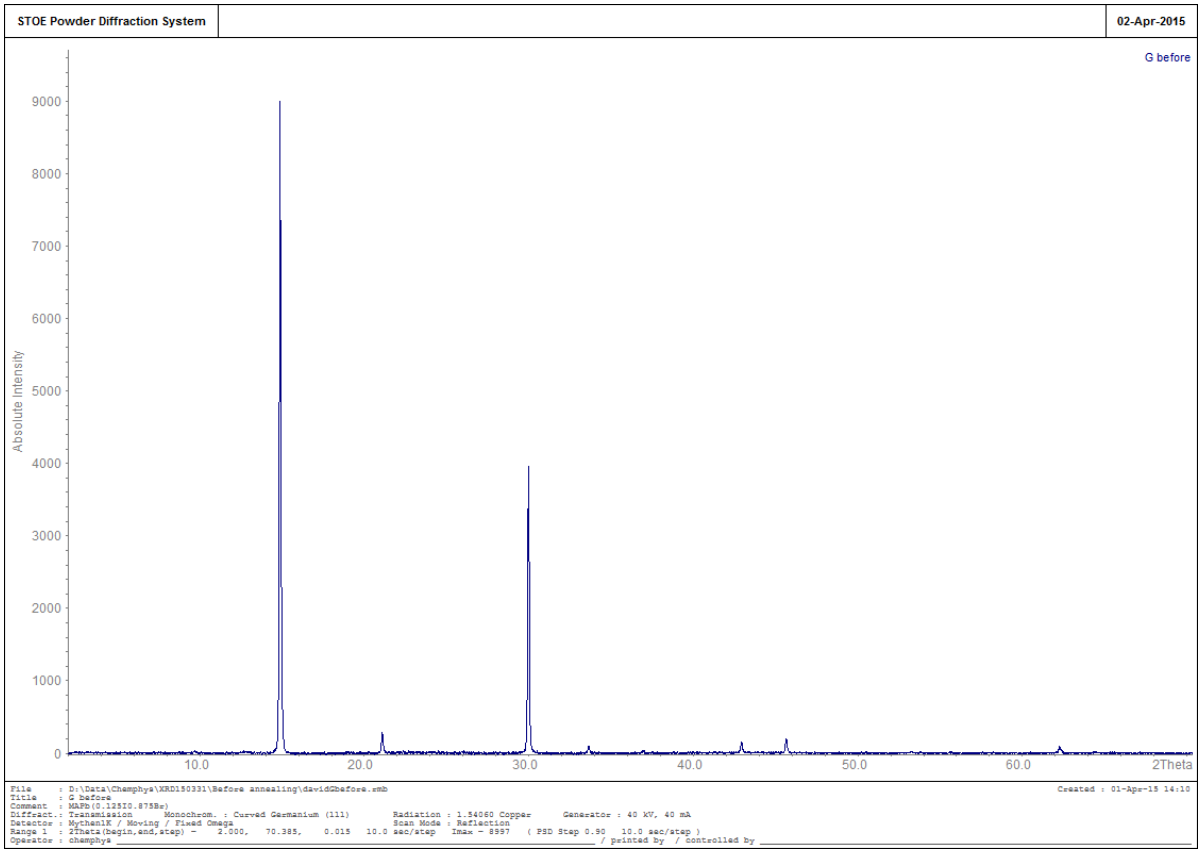

Figure A7. XRD spectrum of sample G before annealing.

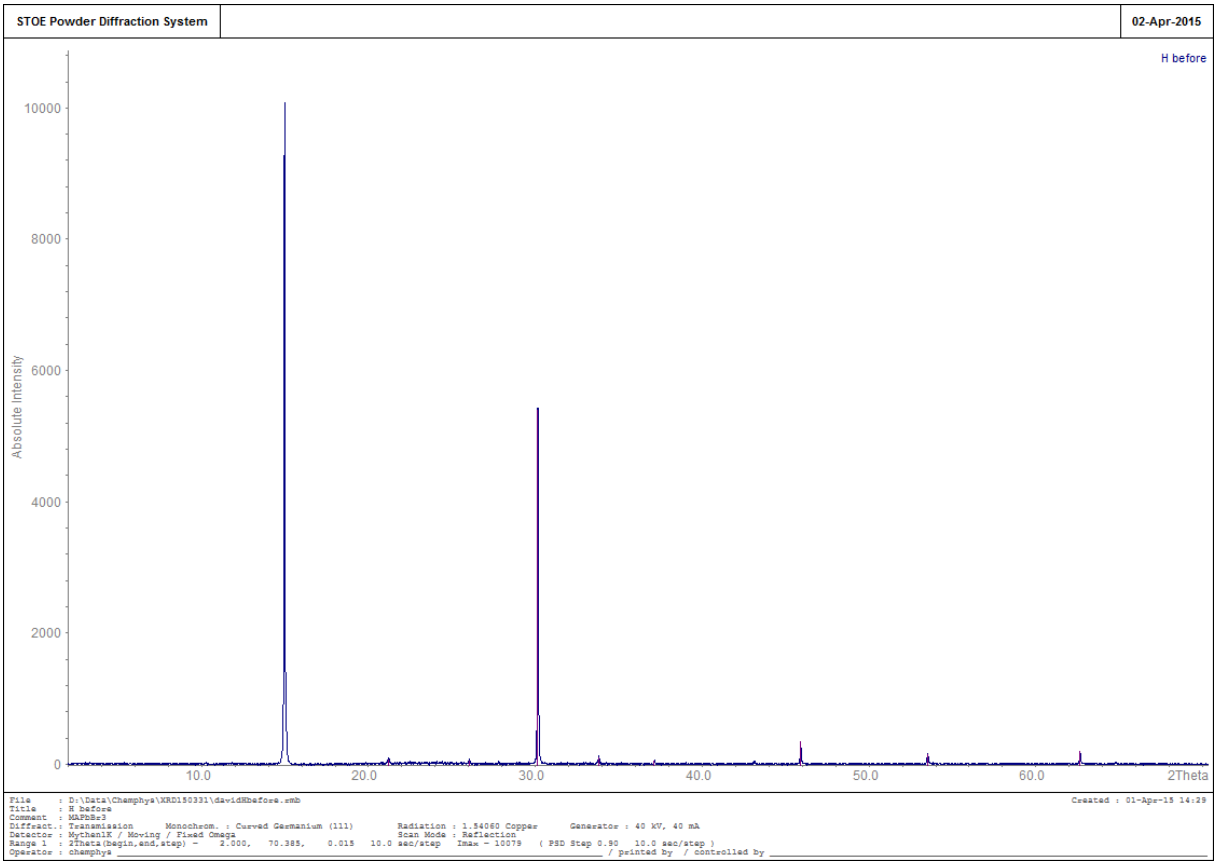

Figure A8. XRD spectrum of sample H before annealing.

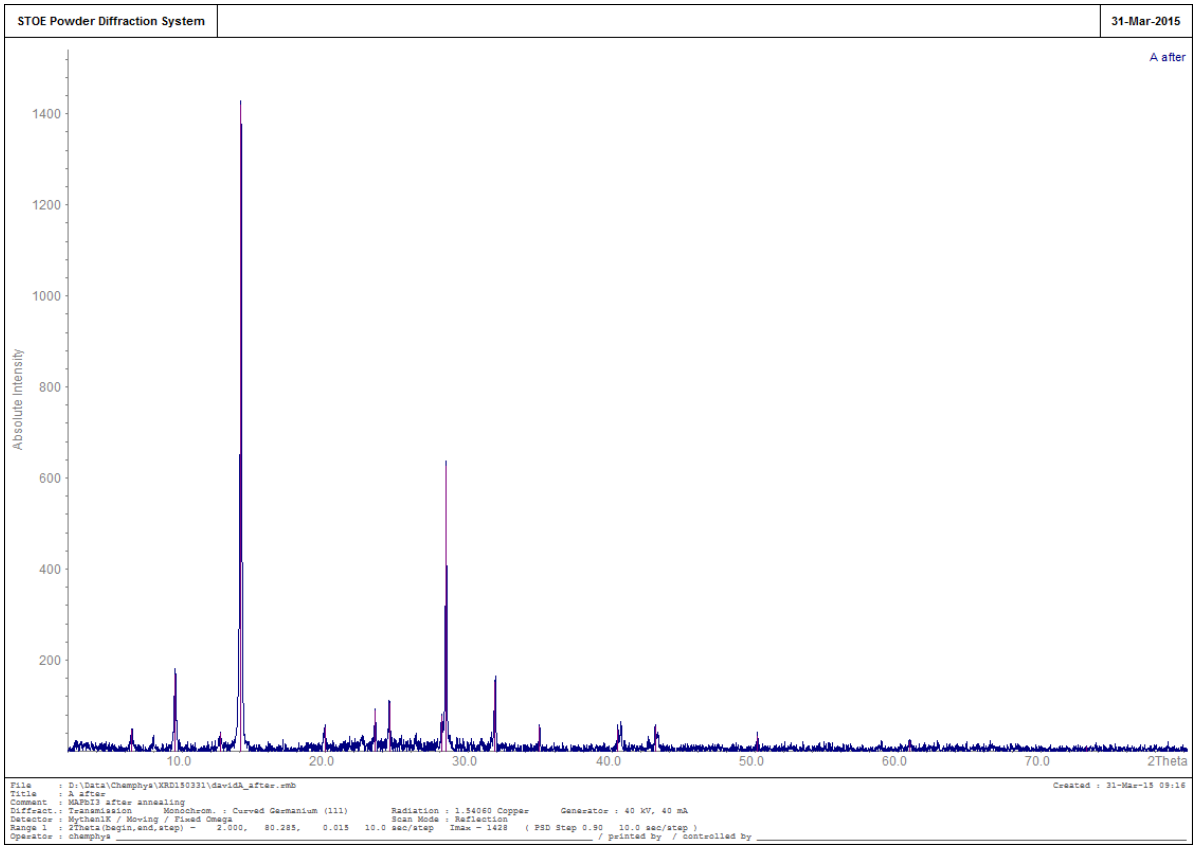

Figure A9. XRD spectrum of sample A after annealing.

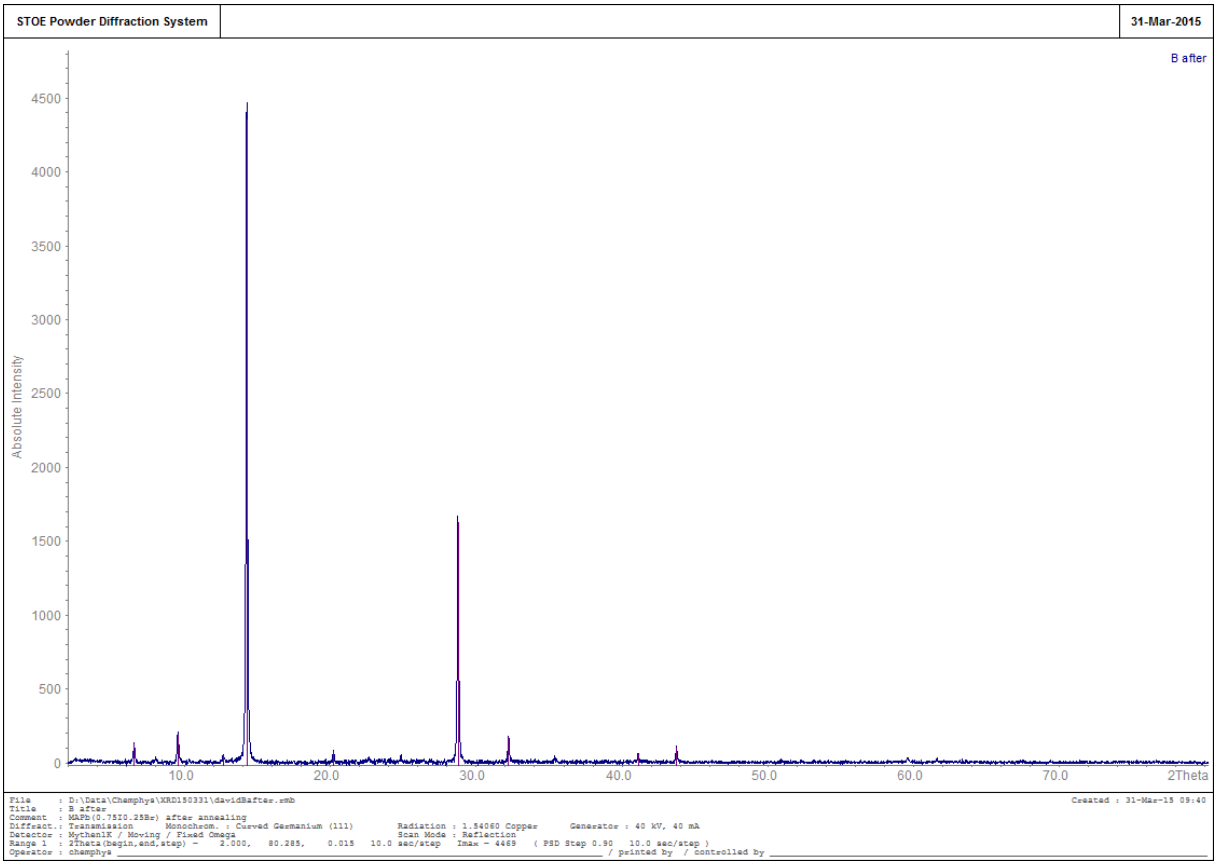

Figure A10. XRD spectrum of sample B after annealing.

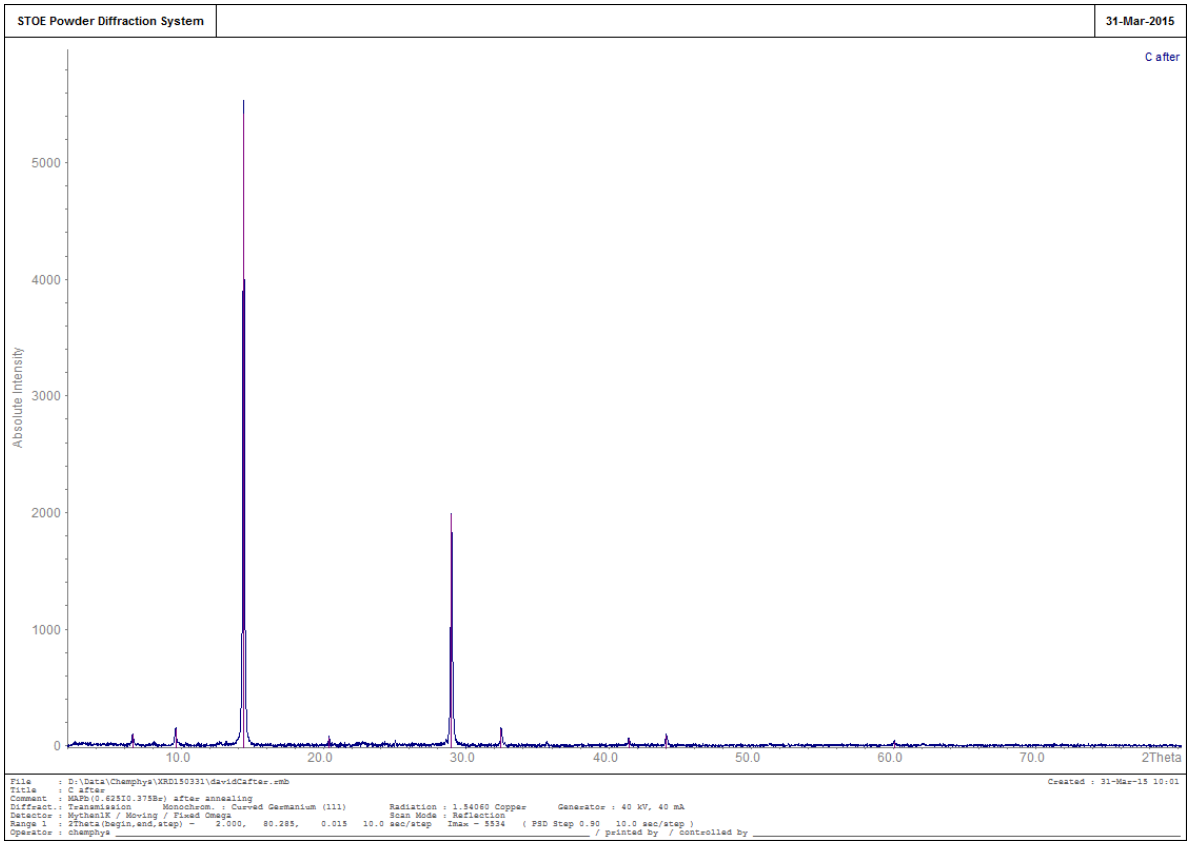

Figure A11. XRD spectrum of sample C after annealing.

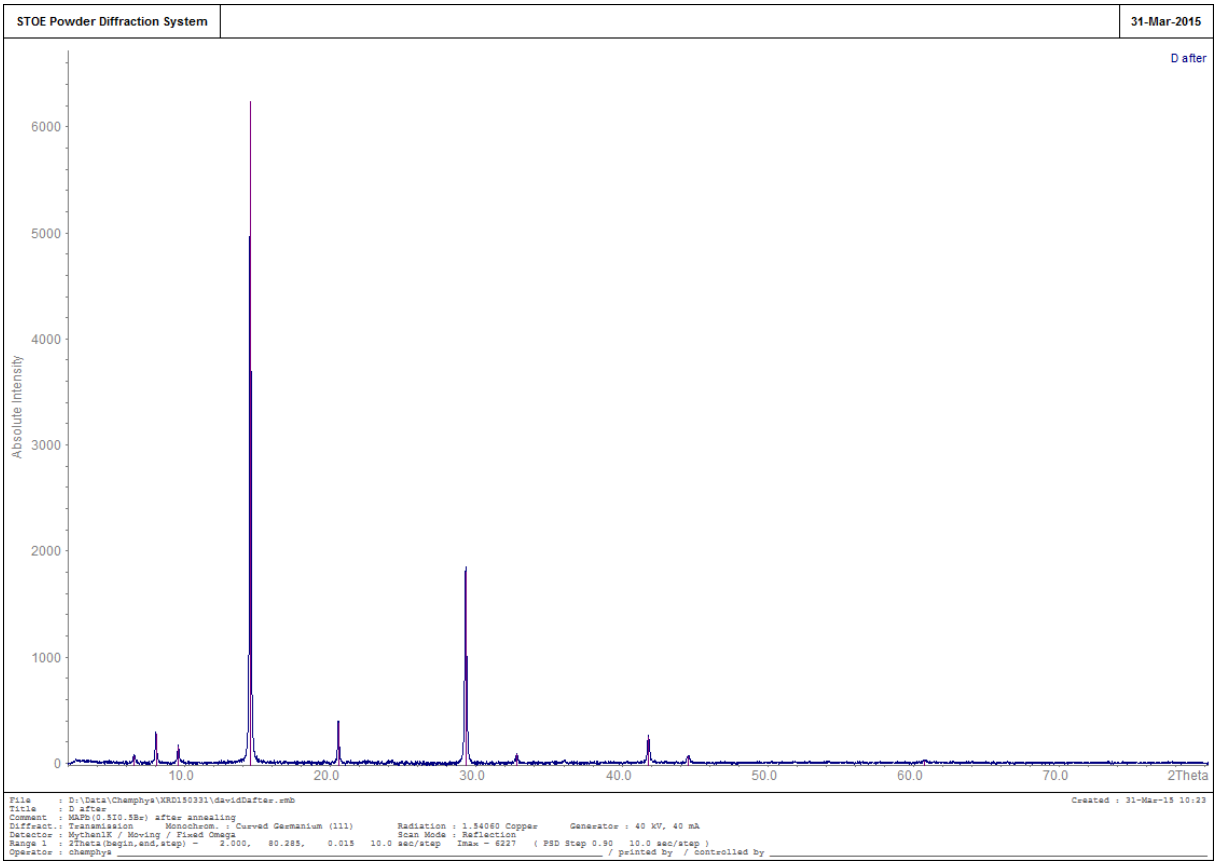

Figure A12. XRD spectrum of sample D after annealing.

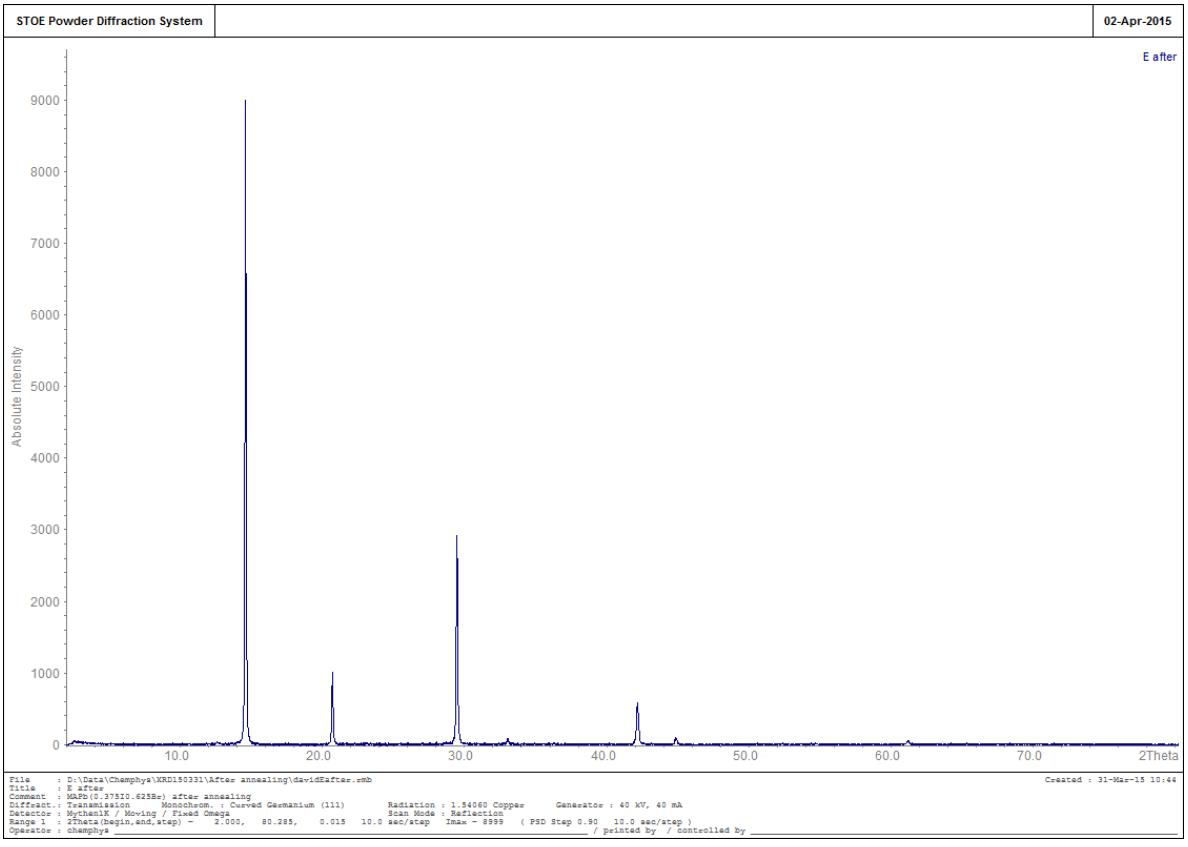

Figure A13. XRD spectrum of sample E after annealing.

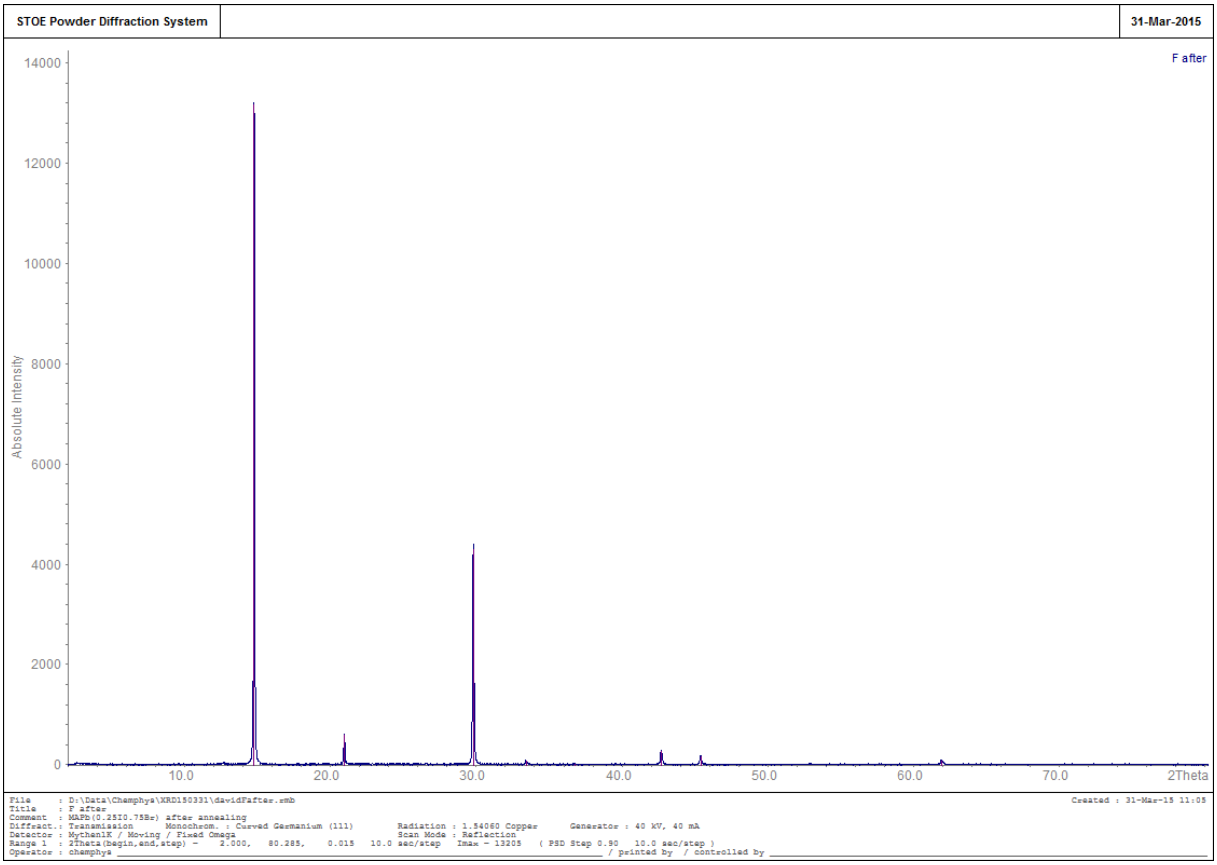

Figure A14. XRD spectrum of sample F after annealing.

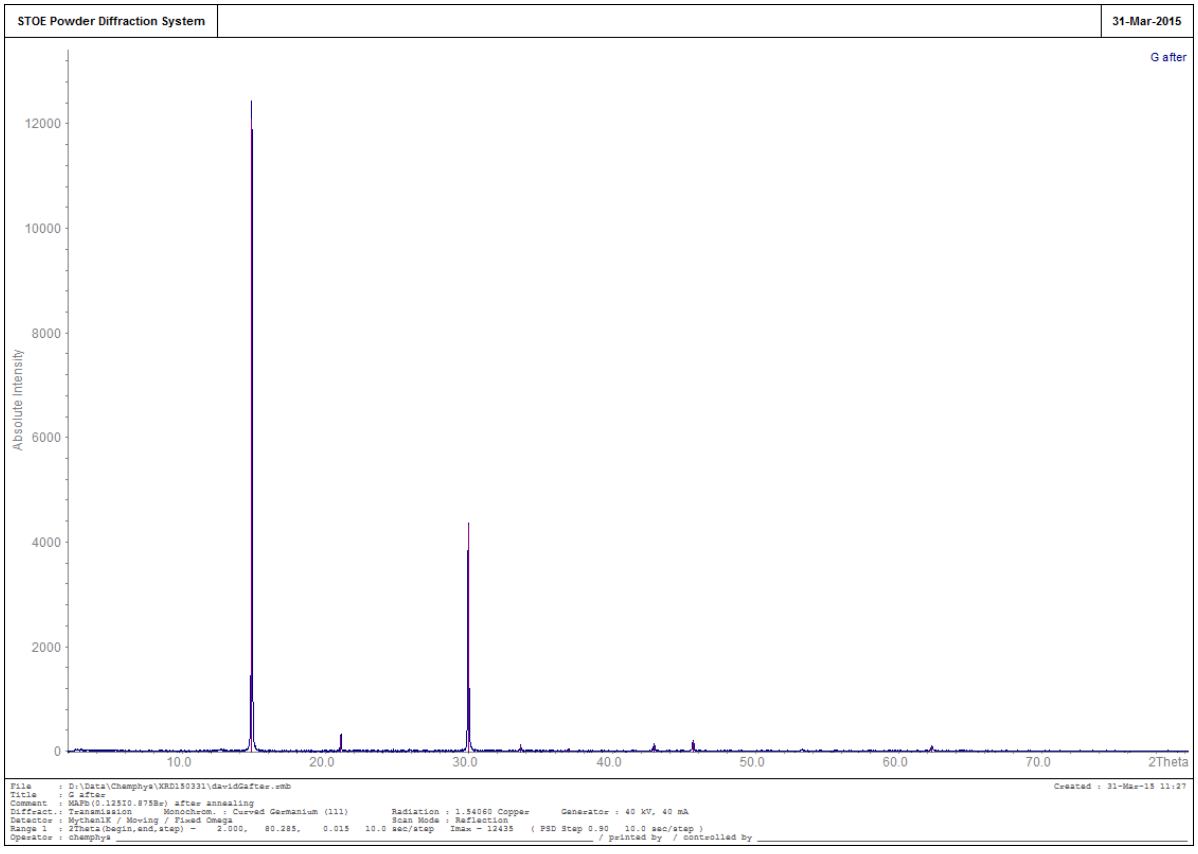

Figure A15. XRD spectrum of sample G after annealing.

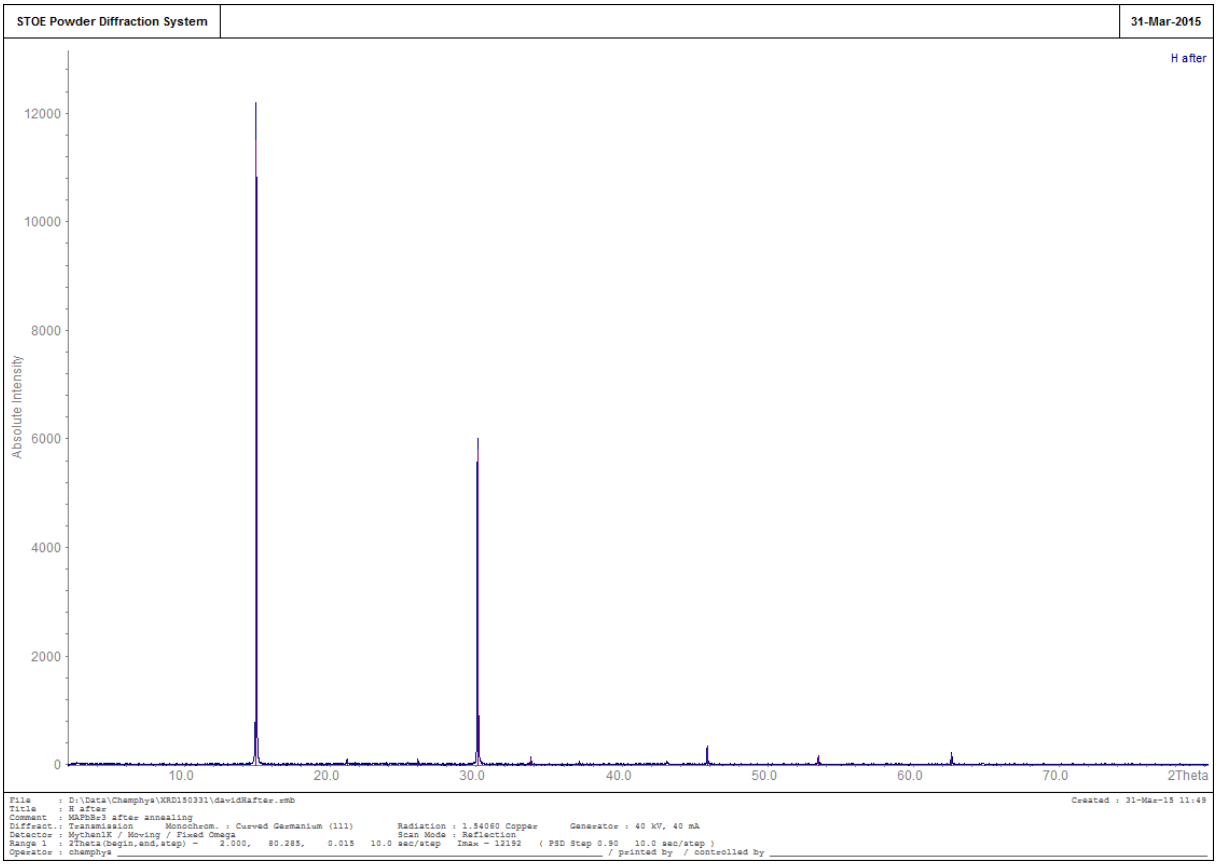

Figure A16. XRD spectrum of sample H after annealing.